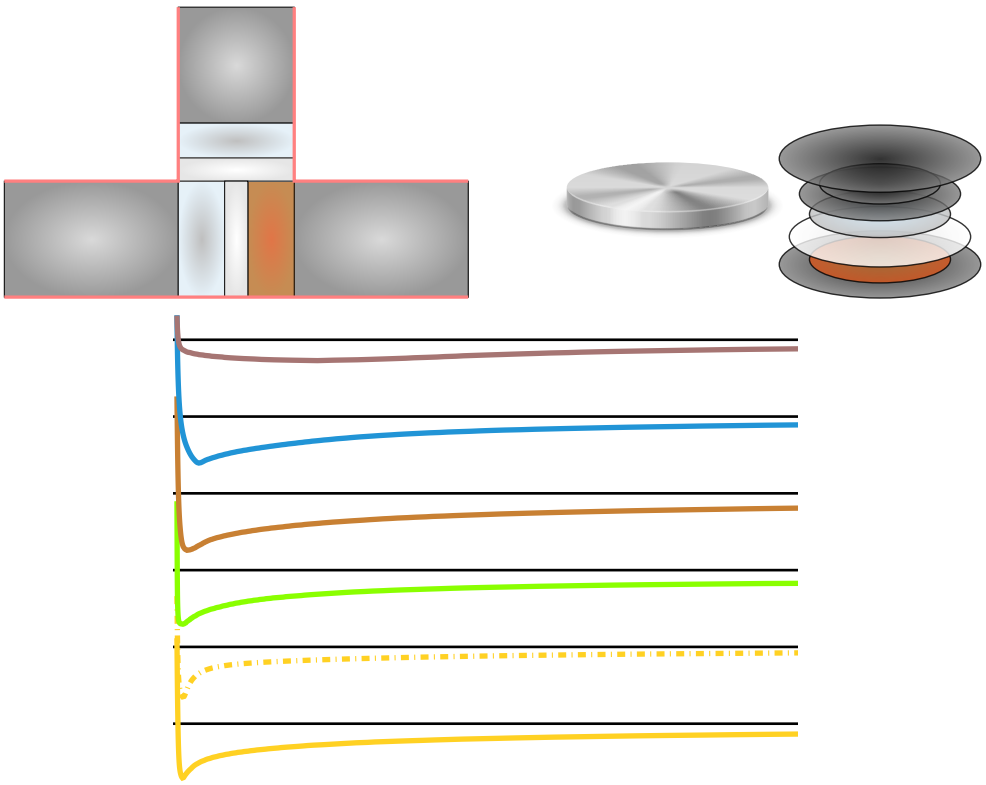
CHALMERS
UNIVERSITY OF TECHNOLOGY



Potassium nucleation and growth

on substrates of disparate potassiophilicity

Master's thesis in Physics

WOJCIECH CHROBAK

DEPARTMENT OF MATERIALS PHYSICS

CHALMERS UNIVERSITY OF TECHNOLOGY
Gothenburg, Sweden 2022
www.chalmers.se

Master's thesis 2022

Potassium nucleation and growth on substrates of disparate potassiophilicity

WOJCIECH CHROBAK



CHALMERS
UNIVERSITY OF TECHNOLOGY

Department of Physics
Division of Materials Physics
Matic group
Chalmers University of Technology
Gothenburg, Sweden 2022

Potassium nucleation and growth on substrates of disparate potassiophilicity
WOJCIECH CHROBAK

© WOJCIECH CHROBAK, 2022.

Supervisor: Josef Rizell, Materials Physics
Examiner: Aleksandar Matic, Materials Physics

Master's Thesis 2022
Department of Physics
Division of Materials Physics
Matic group
Chalmers University of Technology
SE-412 96 Gothenburg
Telephone +46 31 772 1000

Cover: figs. 3.1, 3.2 and 5.10, excluding labels.

Typeset in LaTeX
Printed by Chalmers Digitaltryck
Gothenburg, Sweden 2022

Abstract

The increasing demand for batteries in combination with the limited lithium (Li) reserves has motivated the search for alternatives to the conventional Li-ion battery chemistry. Batteries based on potassium (K) have been proposed due to its greater abundance compared to Li in the Earth's crust. However, the larger weight of K compared to Li necessitates the use of K metal anodes to attain competitive energy densities in K batteries. Metallic anodes are problematic pertaining to rechargeability, as a result of their tendency to form dendritic morphology during cycling. The dendrites are detrimental to the coulombic efficiency of the cells and even hazardous, as they can grow through the separator to the other electrode, causing a short circuit. To control the morphology of K metal, it is imperative to build a fundamental understanding of the electrochemical deposition of K.

This work focuses on studying electrochemical deposition of K metal onto various substrates by method of constant current cycling. With this technique, the voltage response is recorded and the peaks during deposition correspond to the nucleation process. The substrate onto which the metal is deposited affects the nucleation and ostensibly the emerging morphology as a consequence. A surprising result is the similarity in depth of the nucleation peaks for the substrates tungsten (W), previously predicted to be superpotassiophobic and gold (Au), expected to be potassiophilic. Another is the both deeper and wider peak for copper (Cu) as compared to W, even though Cu was theoretically estimated to be over 4 times less potassiophobic.

Keywords — potassium, metal anode, three-electrode, nucleation, overpotential, constant current cycling

Acknowledgements

I would like to express my deepest gratitude to my supervisor, Josef Rizell, without whom I would know next to nothing about this subject. I am extremely grateful to my examiner, Prof. Aleksandar Matic, for his support, not to mention the opportunity to work on this project. Thanks goes out to my opponent, Alexander Engblom, for his apt, yet not overly mean, questions during our discussion.

Everyone I met at Materialfysik was welcoming, helpful and kind. I will remember my time here fondly. Many people helped me with various questions and problems, and I dare not list them all in fear of inadvertently overlooking someone. Even so, I would be remiss to not specifically mention Dr. Nataliia Mozhzhukhina, whose expertise in electrochemistry was invaluable and Dr. Matthew Sadd, whose *Ph.D.* thesis gave me an excellent starting point to immerse myself in this field.

So long, and thanks for all the fi~~sh~~ka!

Abbreviations

Acronyms

BEV battery electric vehicle. 1, 3
CE counter electrode. 7, 8, 14, 15, 17, 19–21, 33
CV cyclic voltammetry. ix, 9, 10, 15, 31, 36
FWHM full width at half maximum. 18, 19, 23, 25, 28, 30
OCV open circuit voltage. 5
RE reference electrode. 7–10, 14, 15, 33
SEI solid electrolyte interphase. viii, ix, 4, 5, 8, 9, 23, 33, 36
SHE standard hydrogen electrode. 3, 22
WE working electrode. 7–9, 14, 15, 17–25, 33, III–V

Chemicals

Ag silver. 12, 14, 15, 17–19, 23, 25, 31, 33
Au gold. v, 12, 14, 15, 17–19, 23–28, 31, 33, III
B boron. 14, 17–19
Cu copper. v, 5, 9, 12, 14, 15, 18, 20, 21, 23–28, 31, 33
C carbon. 1, 2, 10, 35, I
DME dimethoxyethane. 13, 31
Fc ferrocene. 9, 10, 15, 22, 31, 36
    Fc^+ ferrocenium. 9, 10, 15, 22
Fe iron. 10
H_2O water. 13
H hydrogen. 10
In_2O_3 indium(III) oxide. 14, 15, 17–19, 25–29, IV
KFSI potassium bis(fluorosulfonyl)imide. 13
K potassium. i, iii–v, ix, x, 1–5, 7–9, 11–15, 17, 18, 21–25, 27, 29, 30, 33, 37, I–VI
    K^+ potassium cation. x, 4, 17, 21–25, 27, III–VI
Li lithium. v, ix, x, 1–6, 8, 9, 35–37, I
    Li^+ lithium cation. 1, 5
Mg magnesium. 12, 14, 15, 17–19, 23, 25–29, 31, 33, IV
Na sodium. x, 3, II
O_2 dioxygen. 13
PEEK polyether ether ketone. 14
PP polypropylene. 13, 14

Sn tin. 12, 14, 17, 18, 37
W tungsten. v, 12, 14, 15, 17–19, 25–29, 33, V

Symbols

C concentration.
- C_B bulk electrolyte ion concentration. 8
- C_S SEI ion concentration. 8

D diffusivity.
- D_B bulk electrolyte ion diffusivity. 8
- D_S SEI ion diffusivity. 8

F Faraday constant. 8
I current. 22
Q capacity. 9
- Q_C charge capacity. 9
- Q_D discharge capacity. 9

R gas constant. 8
T temperature. 8
V potential, voltage. 5, 17–25, 33, III–V
$\varnothing$ diameter. 14, 15
$\mathcal{V}$ molar volume of metal. 8
$\mathcal{CE}$ coulombic efficiency. v, 9, 26, 28–30
$\Delta_{\mathrm{sol}}H^\infty$ enthalpy of mixing at infinite dilution. ix, x, 7, 11, 12, 17, 25, 29–31, VI
e elementary charge. I, II
i current density. 8
- i_0 exchange current density. 8

m mass. I, II
r radius. 8, 9
t time. 5, 8, 9, 17–21, 23, 25
α charge transfer coefficient. 8
γ interfacial energy. 8
η overpotential. v, x, 2, 8, 9, 18, 23, 25, 27, 29, VI
- η_m minimum[1] overpotential. 9, 18, 27, 29, VI
- η_n nucleation overpotential. 9, 18, 24, 25, 27, 29, 33, III–VI

υ scan rate. 15, 22

[1] *N.b.* that it is not the minimum *per se*, but the least negative

Contents

Abstract **v**

Acknowledgements **vi**

Abbreviations **vii**
Acronyms . . . vii
Chemicals . . . vii
Symbols . . . viii

1 Introduction **1**
1.1 Aim . . . 2

2 Battery materials beyond lithium **3**
2.1 Alkali metal stripping and deposition . . . 3
2.1.1 Dendritic morphology . . . 4
2.1.2 Solid electrolyte interphase . . . 5

3 Theory **7**
3.1 Two- and three-electrode cells . . . 7
3.2 Constant current cycling . . . 8
3.3 Cyclic voltammetry . . . 9
3.4 Enthalpy of mixing at infinite dilution . . . 11

4 Methodology **13**
4.1 Electrolyte . . . 13
4.2 Separators . . . 13
4.3 Potassium metal . . . 13
4.4 Substrates . . . 14
4.5 Two-electrode cells . . . 14
4.6 Three-electrode cells . . . 14
4.6.1 Pretreatment . . . 15
4.6.2 Calibration . . . 15
4.6.3 Cycling . . . 15

5 Results and discussion **17**
5.1 Two-electrode cells . . . 17

5.2 Three-electrode cells 20
5.2.1 Calibration of K/K^+ reference 22
5.2.2 Cycling after potentiostatic hold 23
5.2.2.1 Comparing with enthalpies of mixing 29
5.2.3 Discussion 31

6 Conclusion **33**

Bibliography **35**

A Calculations of theoretical capacities of anode materials **I**
A.1 Pure lithium I
A.2 Lithium intercalated in graphite I
A.3 Potassium intercalated in graphite I
A.4 Pure sodium II
A.5 Pure potassium II

B Supplementary measurement data **III**
B.1 Nucleation peak shapes III
B.2 Absolute overpotentials *vs.* $\Delta_{\text{sol}}H^{\infty}$ VI

1

Introduction

Batteries are an essential part of modern life and there is a constant drive to innovate battery technology. The global battery demand in 2021 reached 580 GW h, more than doubling from 2020 [1]. Current projections for 2030 are in the range of 5 TW h to 9 TW h, mostly due to increased production of battery electric vehicles (BEVs) [1, 2]. Forecasting is never trivial, but the growing battery needs are nonetheless apparent. Improvements are desired in terms of primarily energy density, capacity, cost, safety and sustainability.

Battery cells in general are composed of two electrodes — an anode and a cathode — as well as an electrolyte between them. When charged, there is a difference in potential between the two electrodes. This difference is the driving force for the discharge current. The electrolyte is electronically insulating, but ionically conductive. The electronic insulation prevents spontaneous discharge through the electrolyte, which essentially would mean a short circuit. The ionic conductivity on the other hand is necessary to facilitate the charge transfer, as the electric current through the circuit must be balanced by the ionic current through the electrolyte.

Batteries are commonly classified in two categories: primary and secondary. The difference is that the latter are rechargeable, whereas the former are not. The secondary battery technology most commonly used today is lithium-ion, but technologies using lithium (Li) metal, as well as other elements, are actively explored. The conventional Li-ion anodes work on the basis of intercalation in graphite, the structure of which can be seen in fig. 1.1. The Li cations are reduced and intercalate into the graphite during charging. Contrariwise, during discharge the atoms oxidize back to cations and deintercalate. This half-cell reaction can be summed up as

$$\mathrm{LiC_6} \underset{\text{charge}}{\overset{\text{discharge}}{\rightleftharpoons}} \mathrm{C_6} + \mathrm{Li^+} + \mathrm{e^-}. \tag{1.1}$$

Research into potassium (K) as a potential alternative to Li is interesting due to its comparatively low cost and high abundance. K-ion batteries with anodes based on the same graphite intercalation principle would however not serve as a viable replacement, since the specific capacity would inescapably be significantly lower, as can be seen in appendices A.2 and A.3. Be that as it may, the graphite intercalation anodes in Li-ion or K-ion batteries could possibly be replaced with either Li or K metal electrodes. Such metal anodes would leapfrog intercalation anodes in terms of capacity, the calculations for which can be seen in appendices A.1 and A.5.

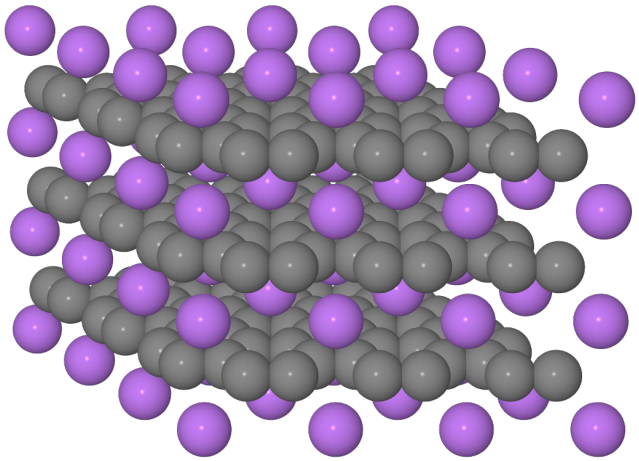


Figure 1.1: Example of graphite intercalation, in this case Li carbide, based on neutron diffraction data in the literature [3, 4, 5]. The model shows LiC_6, which is the highest achievable Li density. For visual clarity the spheres are set to ½ of their van der Waals radii. $3 \times 3 \times 3$ unit cells are displayed, although the actual number and extent of the graphite layers are unbounded. K intercalation is similar, but with a lower maximum density of KC_8. The model is interactive in readers which fully support the PDF 1.6 standard, such as Adobe Acrobat Reader.

The major issue to solve before such batteries could become a reality is the uneven deposition during charging. The dendritic morphology that arises on metal anodes can lead to short-circuiting, as well as a rapid degradation in performance.

Previous studies have shown that the substrate onto which Li is deposited greatly impacts the morphology during stripping and plating [6]. The principal explanation is the differing potential barrier for nucleation for different substrates. Another aspect is the ability of the substrate to form solid solutions with Li [7]. This variation with respect to the substrate seems to not have been investigated as thoroughly for K in particular thus far.

1.1 Aim

The aim of this work was to investigate the process of nucleation of potassium onto different substrates, exploring how the nucleation and growth of K is affected. This has been done by examining the nucleation overpotential during constant current, also known as galvanostatic, cycling. As will be discussed in the following chapter, the nucleation process is critical in terms of the resulting morphology.

2

Battery materials beyond lithium

Li metal has a particularly high theoretical specific capacity of $3861\,\mathrm{mA\,h\,g^{-1}}$ (see appendix A.1 for calculation) compared to $371.9\,\mathrm{mA\,h\,g^{-1}}$ of the common graphite anode for Li-ion, wherein Li intercalates (*cf.* appendix A.2). Apart from superb theoretical specific capacity, Li has a low reduction potential of $\sim -3\,\mathrm{V}$ *vs.* a standard hydrogen electrode (SHE), with some variation depending on the electrolyte [8]. These properties together lay the ground for a remarkably high specific energy of a Li metal battery.

Lithium is not necessarily rare on Earth, but the natural reserves that are economically viable to mine are limited. The total Li resources are estimated at 86 Mt, but possibly viable reserves for mining at only 21 Mt [9]. At a rate of 86 kt mined per year, as in 2019 [9], the reserves would be depleted in under 250 years. Considering the ongoing BEV revolution, it is implausible that the demand would not continue to increase drastically, severely shortening the expected lifetime of the global Li reserves.

Other than lithium, it is possible to use a variety of different elements as the active element in a metal battery. Among them are sodium (Na) and K, which belong to the same alkali metal group as Li. Both Na and K are more abundant than Li. The maximum theoretical capacity, however, is not as high due to their larger atomic masses (see appendices A.4 and A.5) but nevertheless a lot higher than the conventional electrode of Li intercalated in graphite. To achieve such competitive capacities, metal anodes are coveted as a substitute for intercalation due to their unparalleled density of the active element. Thus, Na- or K-based batteries exhibiting highly competitive capacity and cost may yet be developed. Also, since the principles of operation are similar, the discoveries with other elements may prove useful to advance Li technology.

2.1 Alkali metal stripping and deposition

The electrodeposition of Li, K and other alkali metals can be divided into sequential steps, as shown in fig. 2.1. The ions dissociate from their solvation shells, reduce and adsorb as atoms on the substrate, whereafter they electrocrystallize to the bulk [10].

The change in Gibbs free energy associated with the crystallization is highly dependent on the nucleus size. In other words, there is a critical nucleus size under which the crystallization "costs" energy and the process is not spontaneous. Overcoming this

energy barrier, the continued crystallization onto nuclei above the critical size is thermodynamically unimpeded. The energy barrier can be coupled to the voltage response during cycling. The current densities on both electrodes are indubitably important, since they characterize the rate of deposition and thus impact the critical size of nuclei and the voltage barrier for nucleation. More dendritic morphology is correlated with high exchange current densities [10].

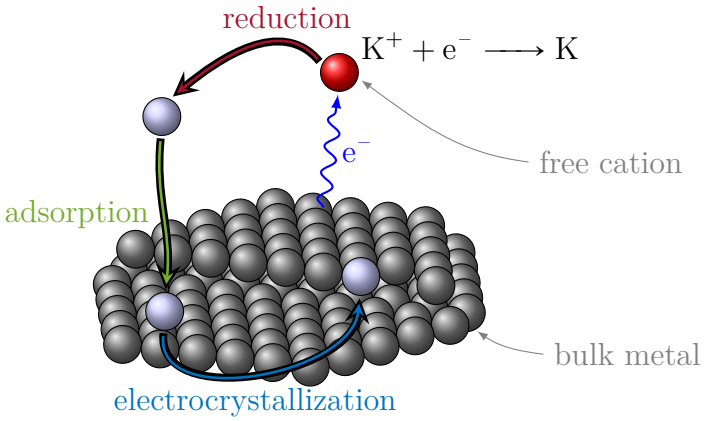
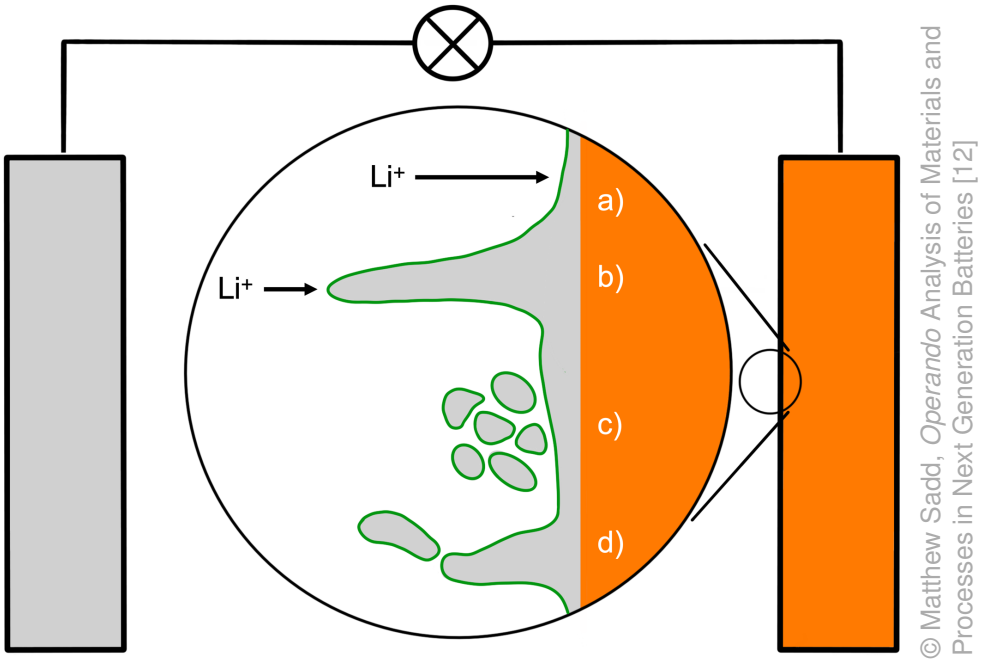


Figure 2.1: Schematic of K metal deposition. The same process applies to other alkali metals. Inspired by figure 1 in [10].

2.1.1 Dendritic morphology

The capacity advantages notwithstanding, metal anodes are problematic in practice. The main issue is the morphology of the metal deposited on the electrode, which usually exhibits a dendritic or porous structure. There are multiple reasons for dendritic formation, such as an inhomogeneous solid electrolyte interphase (SEI), discussed below, resulting in uneven growth, together with a low diffusion rate of ions to the electrode surface compared to their reduction rate. Besides kinetics, deposition onto the already deposited metal may also be thermodynamically favorable compared to the electrode substrate. [11]

A qualitative sketch of possible morphologies can be seen in fig. 2.2. The growing structures may get electronically disconnected and in so doing become inactive, resulting in progressive losses of active material in each cycle, reducing the lifespan of the cell. For this reason, the lithium/potassium in such disconnected structures is commonly called dead lithium/dead potassium. Perhaps more importantly, the dendrites may grow uncontrollably through the separator, resulting in short-circuiting between the electrodes. Accordingly, a naïve implementation of alkali metal anodes constitutes a major hazard.



© Matthew Sadd, *Operando* Analysis of Materials and Processes in Next Generation Batteries [12]

Figure 2.2: Taken from Matthew Sadd's *Ph.D.* thesis [12], with permission. Original caption: "Illustration of various forms of Li metal deposition, in this case on a Cu substrate. a) Ideal Li deposition. b) Deposition leading to dendrite formation. c) 'Dead' Li morphologies. d) Formation of dead Li due to the SEI growing round Li-metal and disconnecting from the bulk."

2.1.2 Solid electrolyte interphase

The organic solvents used as electrolytes with Li and K are by themselves not stable at the potentials used during cycling. The magnitude of the potential necessary for deposition to occur is lower than the ones at which the electrolytes start to break down. In other words, the deposition of Li or K happens outside the electrochemical stability window of the electrolytes. Despite the reactivity, stable SEIs can form by the reductive decomposition of the electrolyte, mostly during the initial charge [13]. However, even when no voltage is applied, *i.e.* at open circuit voltage (OCV), the initial growth is parabolic with respect to time, *i.e.* the thickness follows $\propto\sqrt{t}$ [14]. The SEI acts as a passivating layer, which is ionically conductive but electronically insulating, halting or slowing the breakdown of electrolyte at the electrode.

SEIs have a typical thickness on the order of 10 nm [14]. Near the electrode, the SEI consists of thermodynamically stable, fully reduced, anions, other atoms and their compounds, whereas closer to the electrolyte it consists of a variety of partially reduced materials [14].

The SEI is of interest, not only due to its passivating properties, but also because ionic migration through it is often the rate-determining step of the electrochemical reactions in a cell [14].

3

Theory

The following chapter gives an introduction to some basic electrochemical concepts and techniques used in this study, along with the concept of enthalpy of mixing at infinite dilution and its proposed link to electrochemical wetting.

3.1 Two- and three-electrode cells

For a normal battery cell, only two electrodes are needed, but then solely the potential difference between them can be measured. This is problematic when trying to deduce how the voltage of just one of the electrodes changes when a current flows between the electrodes. When a current is applied, such as in constant current cycling, discussed below, the potential of the counter electrode (CE) may also change, since the reduction process on one of the electrodes must be matched by an equivalent oxidation process on the other. A third, reference electrode (RE) with a stable potential is therefore required to measure the potential of only the working electrode (WE). Otherwise, effects on both the working and counter electrode are measured simultaneously, when only the working electrode is of interest. [15]

The design of the two- and three-electrode cells used in this work can be seen in figs. 3.1 and 3.2, respectively.

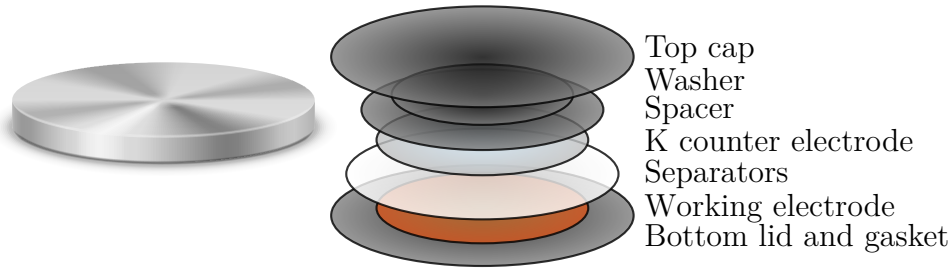


Figure 3.1: Sketch of a two-electrode coin cell. The casing is identical to the one in commercially available CR2032 batteries and looks similar to the drawing on the left. The components inside are all shaped like disks, which are drawn and labeled in order on the right. The separators are wetted with electrolyte.

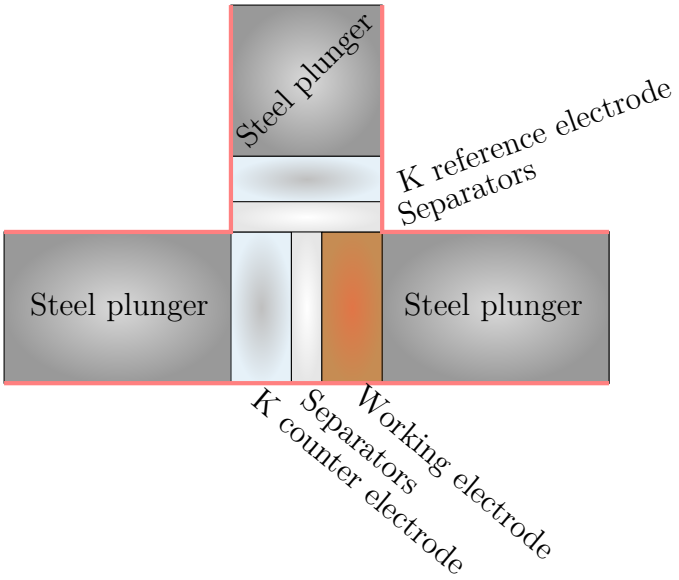


Figure 3.2: Sketch of a three-electrode cell. The separators are wetted with electrolyte and the enclosure is made of plastic.

3.2 Constant current cycling

During a plating half-cycle, a constant current is applied for an extended period of time and the voltage response of the cell is measured. This response is inextricably tied to the so-called overvoltage or overpotential, which is the needed excess potential above what is required purely thermodynamically in order to drive a given electrochemical half-reaction. Next, the current direction is reversed and the stripping half-cycle begins, until a voltage cut-off is reached, completing a full cycle.

By studying this voltage profile, phenomena occurring in the cell can be inferred. As mentioned above, in a three-electrode cell the contributions to the profile from WE and CE can be decoupled. Such a half-cell voltage response during deposition shows the overpotential.

The total overpotential during Li deposition has previously been modeled as

$$\begin{aligned}\eta &= \eta_{\text{charge transfer}} + \eta_{\text{interfacial energy}} + \eta_{\text{bulk diffusion}} + \eta_{\text{SEI diffusion}} = \\ &= \frac{RT}{\alpha F}\ln\frac{i}{i_0} + \frac{2\gamma\mathcal{V}}{Fr} + \frac{irRT}{D_{\text{B}}C_{\text{B}}F^2} + \frac{ir^2RT}{D_{\text{S}}C_{\text{S}}F^2} \quad [16,\ 17].\end{aligned} \tag{3.1}$$

The meanings of all symbols are not essential for the purposes of this work, but they are included in the list of symbols on page viii of the front matter. The combination of inverse, linear and quadratic terms in the radius (r) of the nucleus make it possible to calculate the bulk and interfacial ion transport, given measurements of r and η [16]. A heuristic relation to *e.g.* time, such as $r \propto \sqrt[3]{t}$ during constant deposition, would allow for an estimate of r and thus the aforementioned transport processes.

In reality such a simple relation is not necessarily satisfactory. Three regimes can nevertheless be identified in the measured voltage profiles without having to measure

r, since the minimum $\eta(t)$ corresponds to an extremum with respect to r in eq. (3.1). The three regimes are the SEI formation, the nucleation regime and the growth regime [16], as illustrated in fig. 3.3. The voltage at the minimum is called the nucleation overpotential (η_n), while the voltage at the plateau in the growth regime is — perhaps confusingly — named the minimum overpotential (η_m).

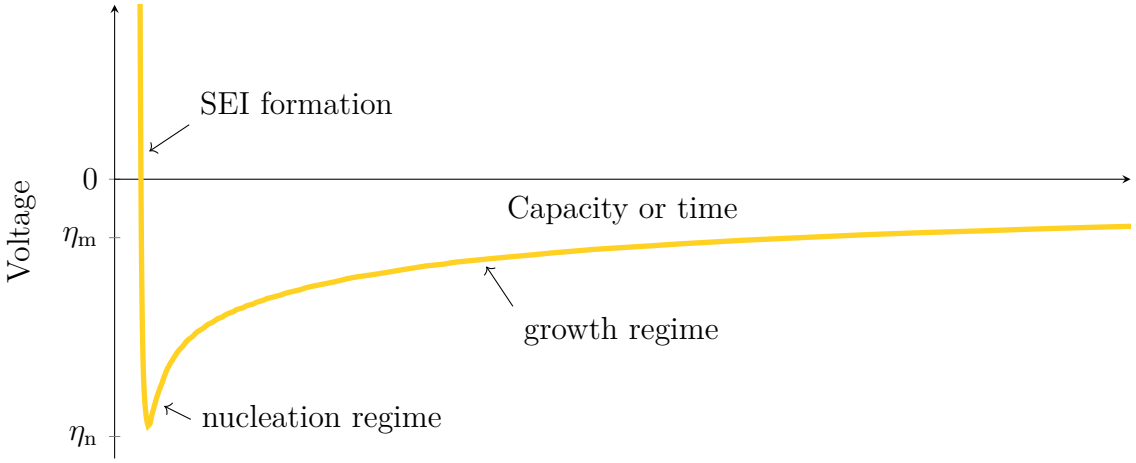


Figure 3.3: Example of overpotential curve during deposition. The nucleation (η_n) and minimum (η_m) overpotentials are marked on the y-axis.

The capacities during charge (Q_C) and discharge (Q_D) can also be measured during constant current cycling, as they are simply the product of the constant currents in each direction and the time during which they can be sustained. Consequently, also the coulombic efficiency,

$$\mathcal{CE} = \frac{Q_\mathrm{D}}{Q_\mathrm{C}}, \tag{3.2}$$

is readily obtainable. The coulombic efficiency can however not be measured for symmetric cells, such as Li-Li or K-K, since there always will be an excess of the active metal on both electrodes, so the loss of material through side reactions or dead Li/K cannot be ascertained and the measured efficiency will always be $\mathcal{CE} \approx 1$. On the other hand, asymmetric cells (*e.g.* K-Cu) cannot strip more of the active metal (K) than was previously deposited on one of the electrodes (Cu), allowing to assess the coulombic efficiency.

3.3 Cyclic voltammetry

Cyclic voltammetry (CV) is an experimental method, whereby a linear potential sweep is performed cyclically between two voltages on the WE with respect to the RE and the resulting current response is measured. It is a powerful electrochemical technique to investigate the reduction and oxidation processes. The current response peaks in one direction of the voltage sweep correspond to specific oxidation processes and reduction processes in the other. This allows for compounds with well-known redox potentials, such as the ferrocene (Fc)/ferrocenium (Fc^+) ion couple, to be

used for calibration of the RE, as the disparity between the measured and expected voltages can be observed. [18]

Ferrocene, which has the formula $Fe(C_5H_5)_2$, is a sandwich complex, as seen in fig. 3.4. Fc is a large molecule with the iron (Fe) atom in the center. Fc^+ has a delocalized charge, lending the Fc/Fc^+ redox potential to be solvent-independent and hence a good candidate for an internal reference [19].

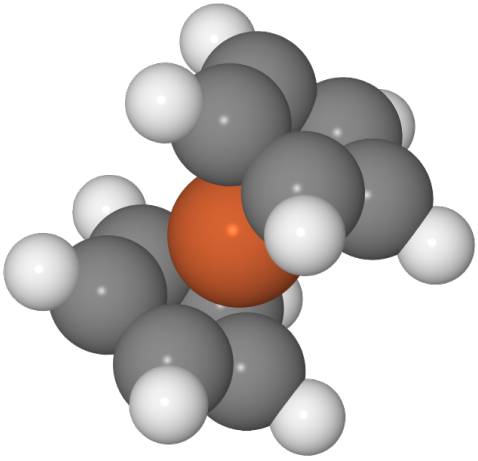


Figure 3.4: Space-filling model of ferrocene, $Fe(C_5H_5)_2$, made with structure data from [20]. For visual clarity the spheres are set to ½ of their van der Waals radii. The model is interactive in readers which fully support the PDF 1.6 standard, such as Adobe Acrobat Reader.

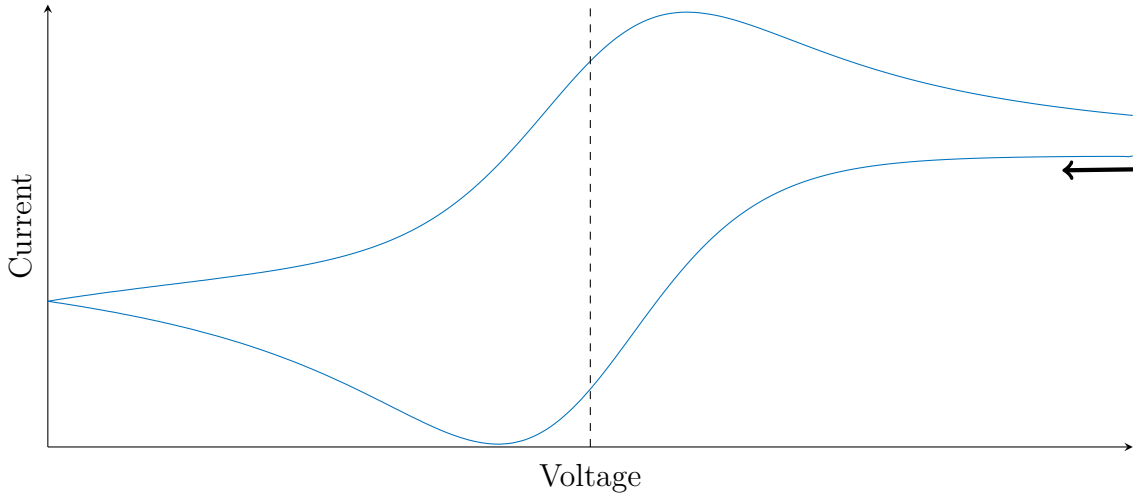


Figure 3.5: Example of a typical CV profile for a one-electron redox system, simulated using tools by Attia [21]. The arrow marks the start and direction of the voltage sweep, whereas the vertical line indicates the redox potential.

The characteristic shape of a CV curve for a one-electron redox system, such as Fc/Fc^+, can be seen in fig. 3.5. The mean of the voltages at the two current extrema is commonly used to determine the redox potential in such a system [18].

3.4 Enthalpy of mixing at infinite dilution

The deposition of K on substrates with different potassiophilicities is studied in this thesis. The selection of substrate materials was based on their enthalpy of mixing at infinite dilution with respect to K, as it previously has been proposed to reflect their potassiophilicity [22]. The enthalpy of mixing at infinite dilution, also called enthalpy of infinite solution ($\Delta_{\text{sol}}H^{\infty}$) is defined as the total theoretical enthalpy change after mixing a fixed amount of solvent in an infinite solution until infinite dilution is reached and no further change in enthalpy can be achieved with mixing. It has been proposed that $\Delta_{\text{sol}}H^{\infty}$ inversely correlates with uniform electrochemical wetting [22]. Figure 3.6 illustrates the idea of the connection of (potassio)philicity, or more specifically wetting, to emerging morphology, whereas fig. 3.7 shows previously calculated $\Delta_{\text{sol}}H^{\infty}$ for a selection of substrates with K.

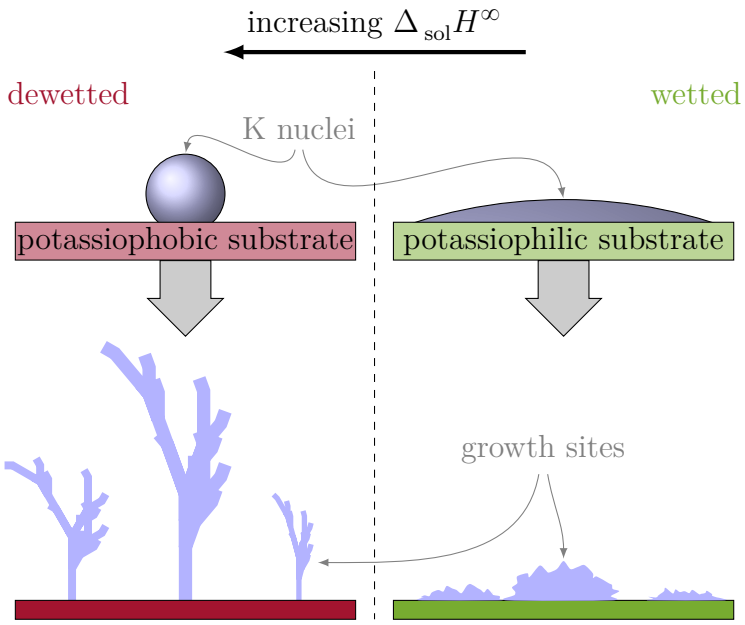


Figure 3.6: Expected relation between enthalpy of mixing at infinite dilution — $\Delta_{\text{sol}}H^{\infty}$, wettability and the emergent morphology during deposition. Redrawn from [22].

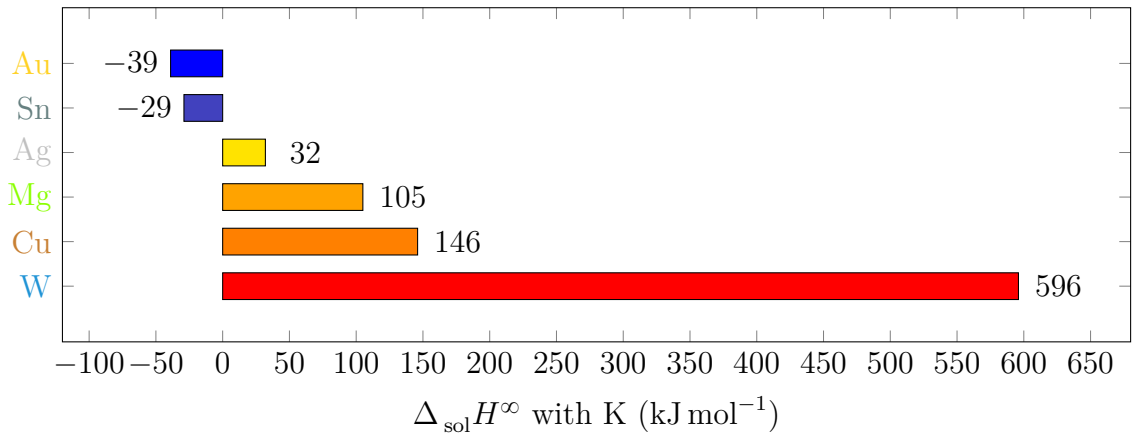


Figure 3.7: Enthalpy of mixing at infinite dilution — $\Delta_{\text{sol}}H^{\infty}$ with K for selected elements. Data taken from [22].

4

Methodology

All relevant procedures, such as assembling cells and preparing the electrolyte and potassium metal, were carried out in argon-filled gloveboxes. During assembly of the majority of three-electrode cells, the atmosphere inside had at most 0.01 ppm O_2 and 0.01 ppm H_2O. The atmosphere during assembly of the prior two-electrode cells was however worse, with H_2O on the order of 1 ppm.

4.1 Electrolyte

The electrolyte used for all experiments was potassium bis(fluorosulfonyl)imide (KFSI) (Solvionic) in dimethoxyethane (DME) (Sigma Aldrich) at a 1 : 2.5 molar ratio. Prior to mixing, the KFSI was dried for more than 48 h under vacuum and the DME was dried over molecular sieves.

4.2 Separators

Two types of separators were used, polypropylene (PP) film, commonly known as Celgard® (2400, Wellcos) and fiberglass filter (Whatman GF/C™, Cytiva). The PP was dried at 40 °C and the fiberglass at 120 °C, both under vacuum.

4.3 Potassium metal

The potassium metal (98 % purity, Sigma Aldrich) was stored in chunks submerged in mineral oil. Firstly, the oil was dried with paper tissues. The outer oxide layer was cut off with a scalpel and discarded. Because the outer layer is very porous, a lot of oil still remained at this stage. Therefore, another layer around the chunks was carved off, but with a separate, clean scalpel. Next, the metal was flattened between two sheets of PP to a thickness of 500 µm, whereafter it was ready to be punched to a desired size. The PP is essential, due to the high reactivity of K towards most other materials.

4.4 Substrates

The investigated substrates were copper (Cu), tungsten (W), tin (Sn), silver (Ag), gold (Au), magnesium (Mg), boron (B) and indium(III) oxide (In_2O_3). Among these, some have been predicted to be potassiophobic and others potassiophilic [22], making the latter good candidates for substrates fostering minimal dendritic morphology. As seen in fig. 3.7, Au and Sn are expected to be some of the most potassiophilic elements, while W ought to be superpotassiophobic, which is why these in particular were chosen for investigation in this work.

The Cu, W and Sn substrates were homogeneous disks, while all others (Ag, Au, Mg, B, In_2O_3) were Cu disks sputtered with the substance in question. All substrates, except for Sn due to its reactivity and mechanical fragility, were cleaned by sonication, first in acetone and then in isopropanol.

4.5 Two-electrode cells

The configuration of the two-electrode coin cells can be seen in fig. 3.1. The substrate disk had a diameter (∅) of 13 mm and the K 10 mm. Two layers of PP, with one layer of fiberglass in between were used as separators, with ∅ = 16 mm. The separators were wetted with 80 µL of the electrolyte.

Cells with Cu, Ag, Mg were cycled ten times each at 59 µA cm^{-2}, counted by the area of the substrate. Separately, cells with every substrate mentioned in section 4.4, except for Cu, were placed at a potentiostatic hold of 0.1 V for 15 min, whereafter a single deposition at 10 µA cm^{-2}, counted by the area of the substrate, was performed.

4.6 Three-electrode cells

The three-electrode cells were of a Swagelok® T connector design, as previously shown in fig. 3.2. The casing was made of polyether ether ketone (PEEK), because it is electrically insulating and chemically inert towards both K and the electrolyte. The inner diameter at the junction between WE and CE was 10 mm. The substrate disks being the WE and corresponding separators thus had the same, ∅ = 10 mm, size. As with the two-electrode cells, it was one fiberglass filter between two PP membranes. The inner diameter at the RE was 6 mm, so instead one small, ∅ = 6 mm, fiberglass separator was placed inside the cavity (directly onto the contact point of WE and CE) and covered by one big, ∅ = 10 mm, PP separator. Sketches of the geometry can be seen in figs. 3.2 and 4.1. The potassium was cut to ∅ = 5 mm (RE) and ∅ = 8 mm (CE), but due to its softness and the pressure during assembly, the resulting sizes were close to ∅ = 6 mm and ∅ = 10 mm.

In the interest of time, the potassium of the CE and RE was reused for consecutive experiments, but with all other parts replaced, including the casing and all separators. The fresh separators were wetted with 90 µL of the electrolyte in total during reassembly.

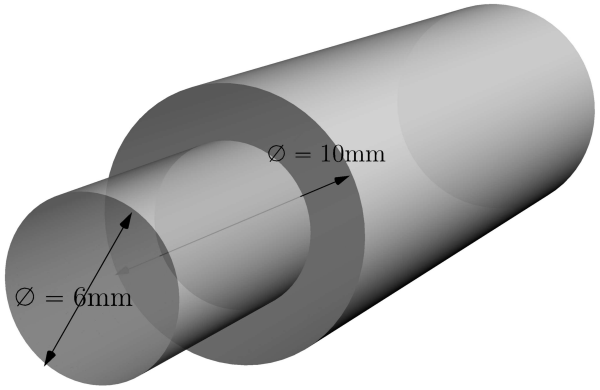


Figure 4.1: The geometry of the RE current collector. *Cf.* fig. 3.2. The WE and CE current collectors consist of single ∅ = 10 mm cylinders. The model is interactive in readers which fully support the PDF 1.6 standard, such as Adobe Acrobat Reader.

4.6.1 Pretreatment

The reference electrodes used were also made of K, which could have been problematic, due to its high reactivity and therefore unstable rest potential. To mitigate the instability, the potassium was pretreated with a plating-stripping process [23]. This was done by arranging the two potassium electrodes to face each other and passing a current of 17.4 µA cm^{-2}, counting with the RE ∅ = 6 mm, for 10 h, once in each direction.

4.6.2 Calibration

The reference potential in a three-electrode cell should be calibrated with a reliable redox reference [15]. In literature, a recommended reference system is the Fc/Fc$^+$ ion couple [24], which was therefore used in this study. Three-electrode cells with pretreated K RE and CE, as discussed above, although only the steel plunger as WE were used with the same separators and electrolyte, but with the addition of Fc, resulting in a concentration of ∼ 5 mM Fc. CV scans were performed with various voltage limits and scan rates (υ), but the most useful were in the range 2 V to 4.5 V with $\upsilon = 2\,\mathrm{mV\,s^{-1}}$.

4.6.3 Cycling

For three cells each with Cu, Ag and Mg as substrates a small current of 9 µA cm^{-2} was applied for 10 h, then ten cycles of 0.36 mA cm^{-2}, both counted by the area of the substrate, in each direction were performed for 6 min or until a cutoff voltage was reached. Cells with Cu, W, Ag, Au, Mg and In_2O_3 were also placed under a potentiostatic hold at 0.05 V for 15 min *vs.* the reference potential. Subsequently, ten cycles were performed, consisting of 0.36 mA cm^{-2} in each direction for 6 min or until a cutoff voltage was reached. As above, the current density was counted by area of the substrate.

5

Results and discussion

In this chapter the results of the study are presented, starting with the two-electrode cell data. The necessity for of a third electrode is demonstrated and calibration data are presented. Finally, data are analyzed in relation to $\Delta_{\text{sol}}H^{\infty}$ of the substrates.

5.1 Two-electrode cells

The potential profiles during the single depositions at $10\,\mu\text{A}\,\text{cm}^{-2}$ can be seen in fig. 5.1. In order to better see and compare the shapes of the nucleation peaks, the first ten minutes are shown in fig. 5.2, with only one sample of each substrate for the sake of clarity.

Unlike the other substrates, Sn does not exhibit a similar nucleation peak. This is due to Sn alloying with the deposited K around 0.2 V *vs.* K/K^{+} [25]. In hindsight, studying K nucleation on Sn would either require a larger current or first completing the alloying process, forcing metallic K to be deposited onto the alloy.

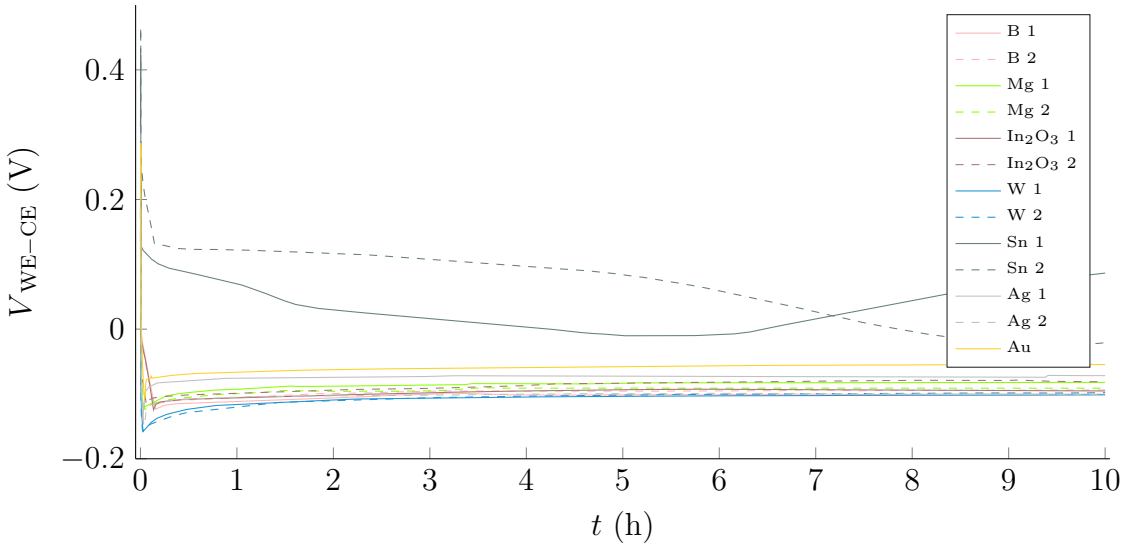


Figure 5.1: Potentials recorded during deposition at $10\,\mu\text{A}\,\text{cm}^{-2}$. *Cf.* fig. 5.2.

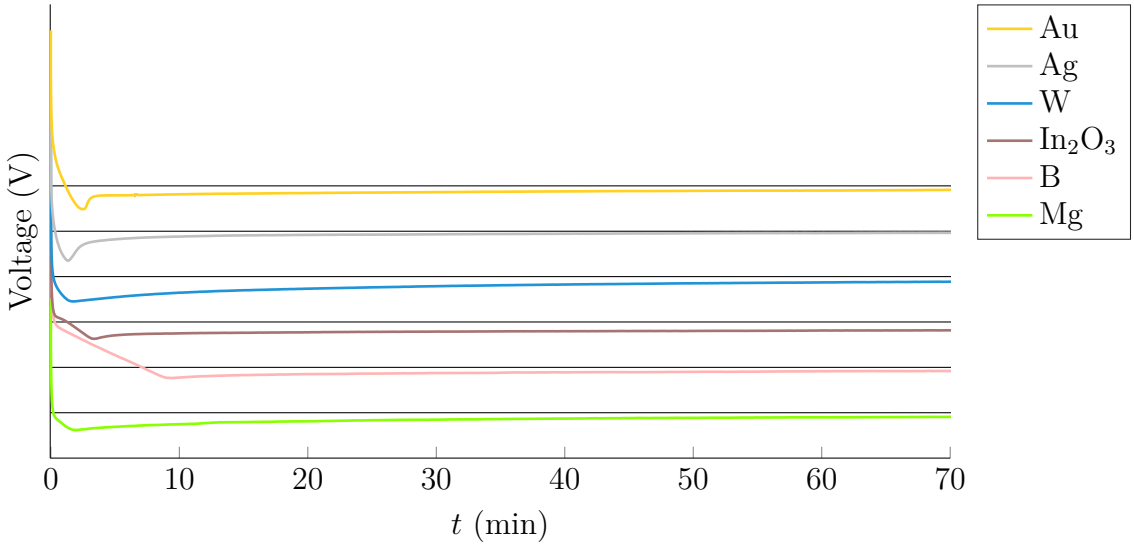


Figure 5.2: First 70 min of deposition for one sample of each substrate except Sn at $10\,\mu A\,cm^{-2}$, showing the nucleation peak. Data are vertically offset for clarity and the horizontal black lines correspond to voltages attained at the end of the deposition for each sample. More precisely, reference heights are set to equal the time average $\overline{V(t > 333\,\text{min})}$. The distance between two neighboring horizontal lines equals to 0.2 V. *Cf.* fig. 5.1.

The relative depths and full widths at half maxima (FWHMs) were extracted as shown in fig. 5.3 and are presented in table 5.1. These depths correspond to $\eta_m - \eta_n$, *i.e.* the difference between the minimum and nucleation overpotentials, *cf.* fig. 3.3. Looking merely at the depths and comparing with fig. 3.7, the similarity between W ((57 ± 2) mV), thought to be superpotassiophobic, and Au (51 mV), and Ag ((58 ± 7) mV) is quite striking. The difference in FWHM is nonetheless clear, with the nucleation peak of W being an order of magnitude broader. It is also interesting that, barring W, the nucleation peaks of Au and Ag are the deepest among all substrates in the data set, although they are also the narrowest.

The voltage profile of one of the Cu coin cells cycled at $59\,\mu A\,cm^{-2}$ can be seen in fig. 5.4. Disregarding the first cycle, a second, much broader peak appears after every nucleation peak, but it is not due to any processes directly on the WE, as will become apparent in section 5.2. These potential steps could correspond to stripping freshly deposited K *vs.* pitting from the bulk K, as solely the bulk K is present in the first cycle.

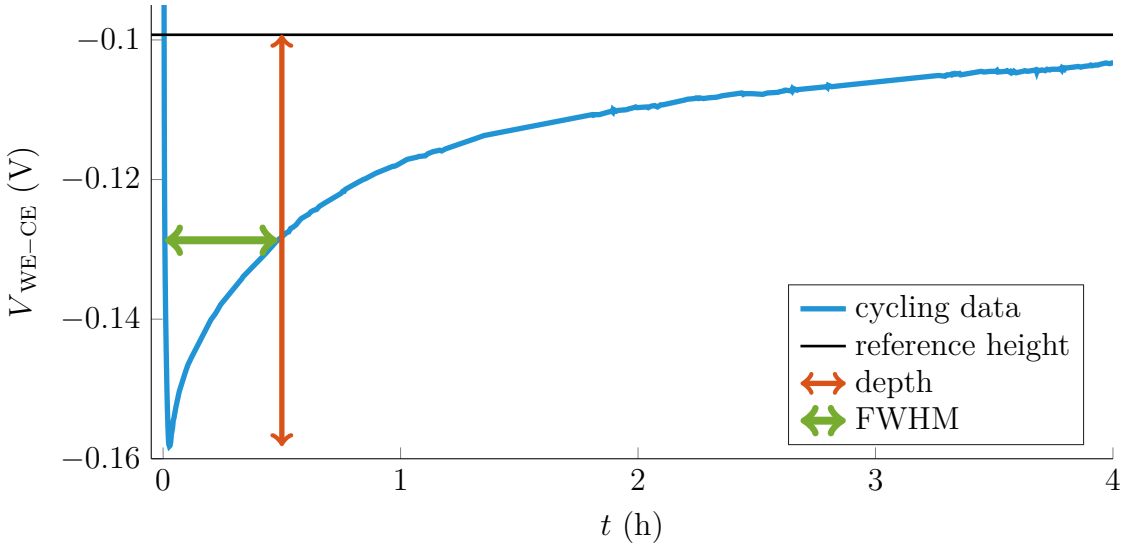


Figure 5.3: Example of peak depth and FWHM extraction from the cycling data, in this case a slow deposition onto W at $10\,\mu\mathrm{A\,cm^{-2}}$ for a total of 10 h. The reference height is placed where the slope has tapered off, here the time average $\overline{V(t > 333\,\mathrm{min})}$ was chosen as reference.

Table 5.1: Relative depths and FWHMs of the nucleation peaks for the single deposition after a potentiostatic hold. Substrates are sorted by average depth in ascending order.

	Peak depth [V]	FWHM [min]
B	0.023	27.2
	0.024	45.0
In_2O_3	0.030	12.9
	0.037	64.7
Mg	0.033	19.3
	0.038	18.7
Au	0.051	1.6
W	0.055	18.4
	0.059	28.5
Ag	0.051	2.1
	0.065	1.7

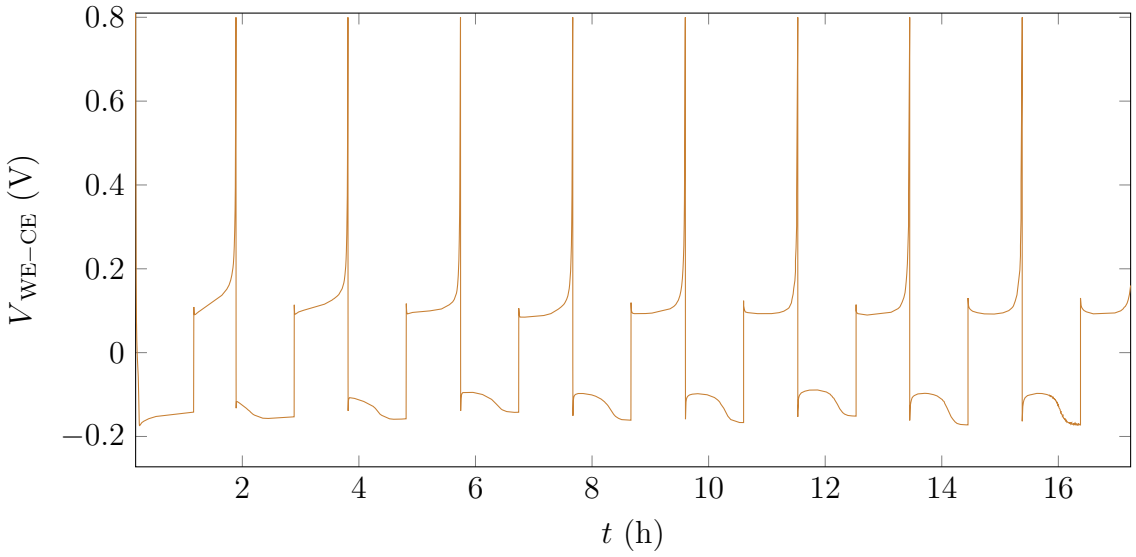


Figure 5.4: Voltage response for a two-electrode cell with Cu as WE, cycled at $59\,\mu\mathrm{A\,cm^{-2}}$. Note the broad dips after the nucleation peaks appearing in all cycles barring the first. *Cf.* the voltage responses $V_{\mathrm{WE-CE}}$ and V_{WE} in a three-electrode cell with a Cu WE in fig. 5.5.

5.2 Three-electrode cells

An example of the three measurable voltage profiles during cycling of a three-electrode cell is in fig. 5.5. As with the two-electrode cell from fig. 5.4, the WE substrate was Cu. The dip after the nucleation peak can be observed in $V_{\mathrm{WE-CE}}$, but vanishes in V_{WE}, which is the relevant potential for studying processes on WE. The cause of the feature can be seen in V_{CE}, which experiences a potential drift when polarized. Aside from the broad dip, it can also clearly be seen that V_{CE} exhibits a sharp peak coinciding with the nucleation peak, further demonstrating that two-electrode cells are not suitable for studying this phenomenon.

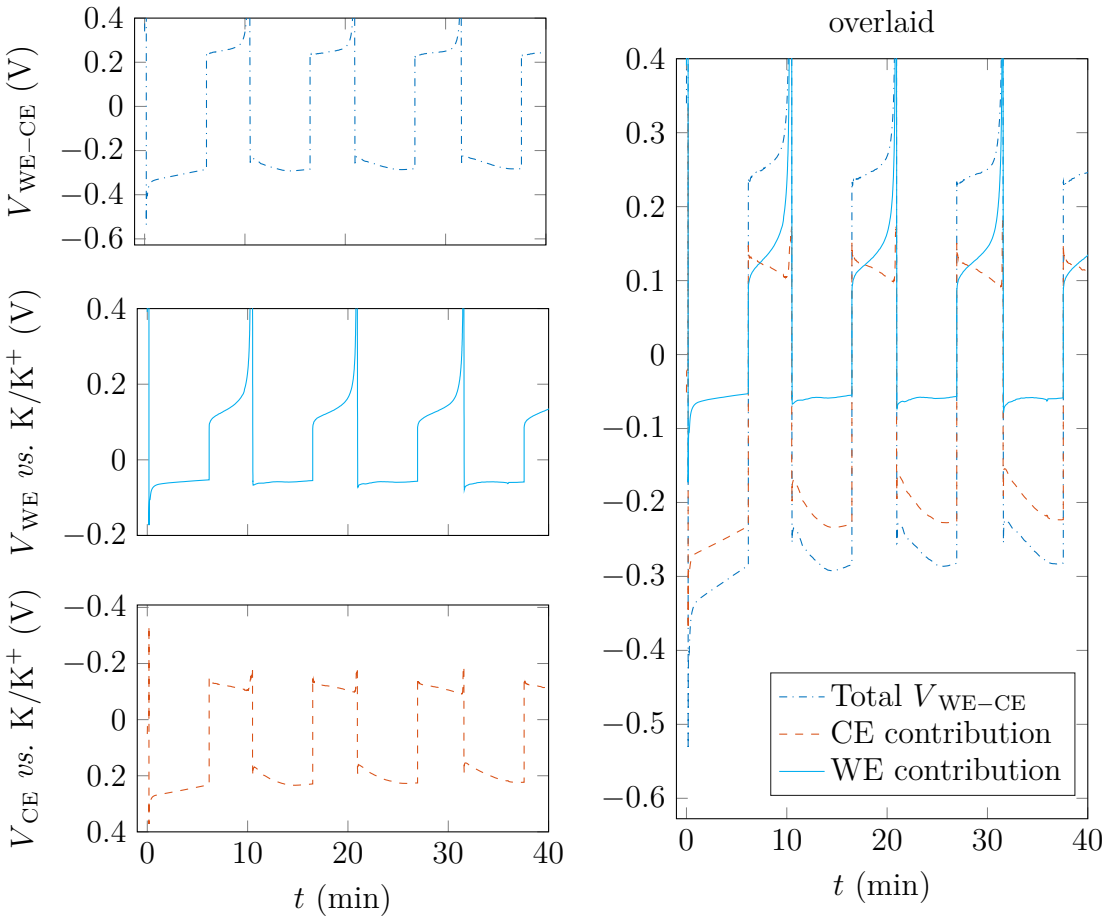


Figure 5.5: Voltage responses $V_{\mathrm{WE-CE}}$, V_{WE} and V_{CE} during constant current cycling at 0.36 mA cm^{-2} of a three-electrode cell with a Cu WE. Note that the y-axis for V_{CE} is flipped in order to more easily compare it with $V_{\mathrm{WE-CE}}$. *Cf.* fig. 5.4.

5.2.1 Calibration of K/K^+ reference

Results of one of the more successful attempts at calibration of the K reference is shown in fig. 5.6. The peaks are not as pronounced as one would have hoped, but they do match the expected voltage. The procedure was vexing, as the failure rate of cells was high and peaks other than the Fc/Fc^+ one were often more prominent at higher scan rates. Higher scan rates also result in higher ohmic drop, giving a larger separation between the reduction and oxidation peaks. On the other hand, lowering the scan rate leads to less prominent peaks in general. Higher voltages also caused breakdown of the electrolyte, as evidenced by a high resulting current. Nevertheless, in the more successful attempts the peaks corresponding to Fc that were recorded were stable.

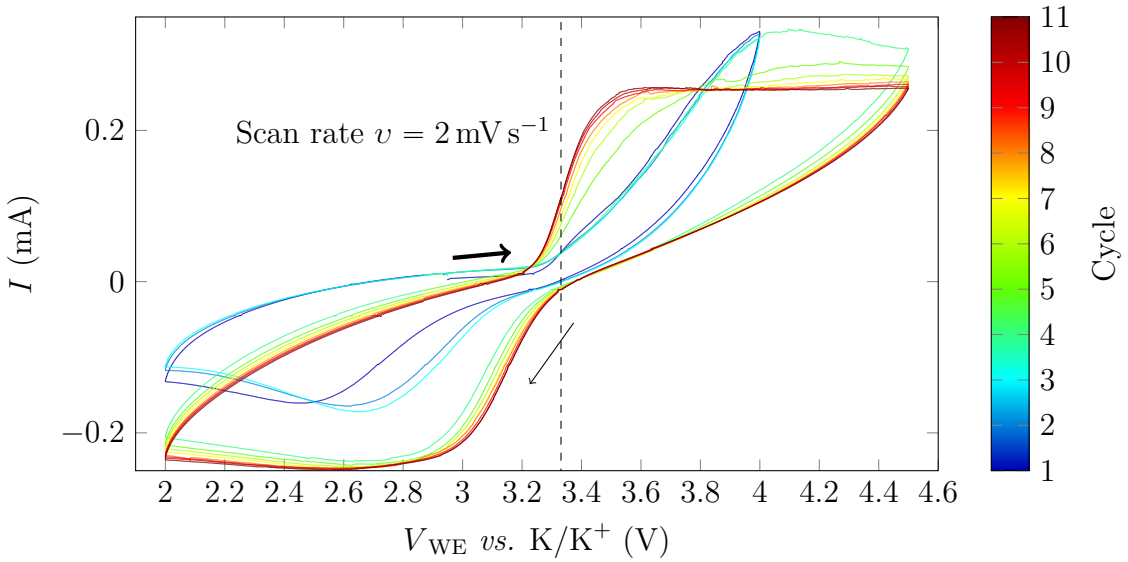


Figure 5.6: Cyclic voltammetry scan with $\sim 5\,\mathrm{mM}$ Fc at $\upsilon = 2\,\mathrm{mV\,s^{-1}}$. The WE consisted solely of the steel plunger. 11 cycles were performed in total, starting in the range 2 V to 4 V. After the 2nd cycle the upper limit was raised to 4.5 V. Arrows indicate cycling direction, of which the thicker is placed near the starting point of the first cycle. The vertical line indicates $V = 3.331\,\mathrm{V}$, the expected reduction potential of Fc.

Taking the average of the voltages at the global current extrema, *i.e.* over all 11 cycles in fig. 5.6, 3.35 V is obtained. Restricting the analysis to individual cycles, it can be seen that only cycles 4, 5 and 6 attain maxima before the cut-off voltage of 4.5 V. A more sophisticated analysis of the signal would therefore be needed. Nevertheless, the average of the voltages at the extrema for cycles 4, 5 and 6 are 3.12 V, 3.05 V and 3.05 V, respectively. The theoretically expected reduction potential is 3.331 V and is obtained in the following fashion. Relevant standard reduction potentials, *i.e.* reduction potentials *vs.* SHE found in literature are $-2.931\,\mathrm{V}$ for $K^+ + e^- \rightleftharpoons K$ and $0.400\,\mathrm{V}$ for $Fc^+ + e^- \rightleftharpoons Fc$ [26]. The expected reduction potential for Fc *vs.* K/K^+ is then $V_{\mathrm{Fc/Fc^+}-\mathrm{K/K^+}} = V_{\mathrm{Fc/Fc^+}} - V_{\mathrm{K/K^+}} = 3.331\,\mathrm{V}$.

5.2.2 Cycling after potentiostatic hold

Cells were placed under a potentiostatic hold to induce the formation of the SEI before cycling, due to the SEI formation step, as seen in fig. 3.3, smearing out the nucleation peak. The overpotential for one such Cu cell is displayed in fig. 5.7. The galvanostatic cycling settings themselves were identical to the ones in fig. 5.5, but the effect of the potentiostatic hold can clearly be seen. The nucleation peaks are deeper, ergo the FWHMs are smaller, yet the nucleation regime (*cf.* fig. 3.3) is wider overall. For visual clarity, nucleation peaks from fig. 5.7 are also shown overlaid onto each other in fig. 5.8.

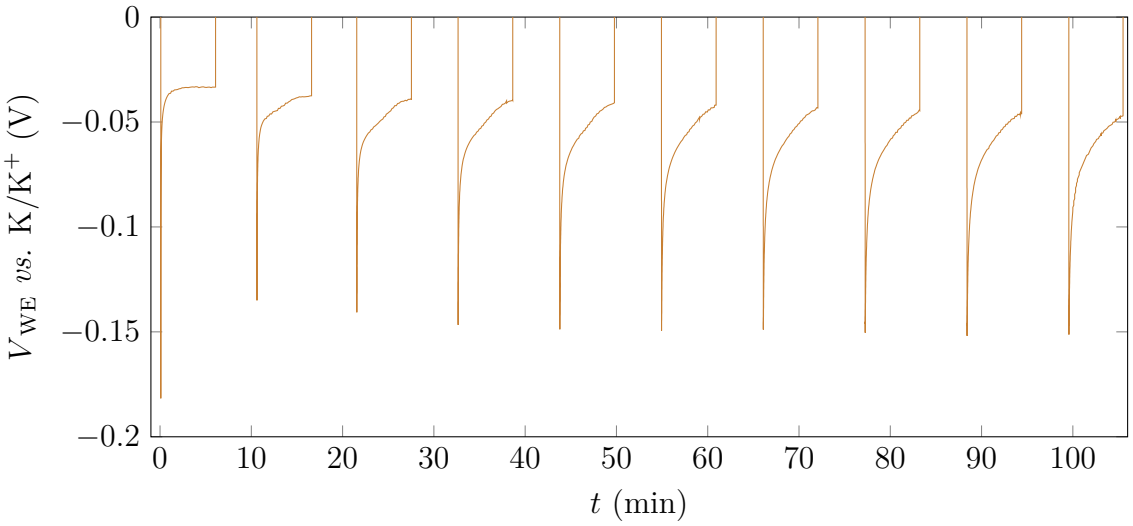


Figure 5.7: Overpotential of a Cu cell cycled at $0.36\,\mathrm{mA\,cm^{-2}}$ after a potentiostatic hold at 0.05 V for 15 min. *Cf.* figs. 5.5 and 5.8.

Similarly, the peaks for one of the Au samples are shown in fig. 5.9 and data for other substrates are included in appendix B.1. In later cycles the Au samples exhibit secondary, much broader and delayed minima. The prominence of this secondary minimum tends to grow with each cycle. This could possibly indicate Au alloying with K or perhaps secondary K nucleation onto the Cu surface underneath, if some of the sputtered Au were to delaminate during the stripping half-cycles. The Mg sample also exhibits secondary peaks, as seen in fig. B.3, but on the order of only 1 s after the primary peaks and they do not grow in prominence after the 2$^{\mathrm{nd}}$ cycle.

The first nucleation peak of K for each substrate is shown in fig. 5.10. On Ag no nucleation peak could be detected in the first cycle, since $\dot{V} \leqslant 0, \ddot{V} \geqslant 0$ for the whole duration, *i.e.* there was no local dip in the voltage response for the first cycle. Peaks did occur in subsequent cycles, though it must be acknowledged that the cell underwent momentary open circuits during cycles 2 and 7. Even so, a similar behavior with no nucleation peak in the first cycle was observed for one out of three earlier cells with Ag WEs without a prior potentiostatic hold. This suggests that either the usual nucleation process does not always occur on Ag during the first cycle

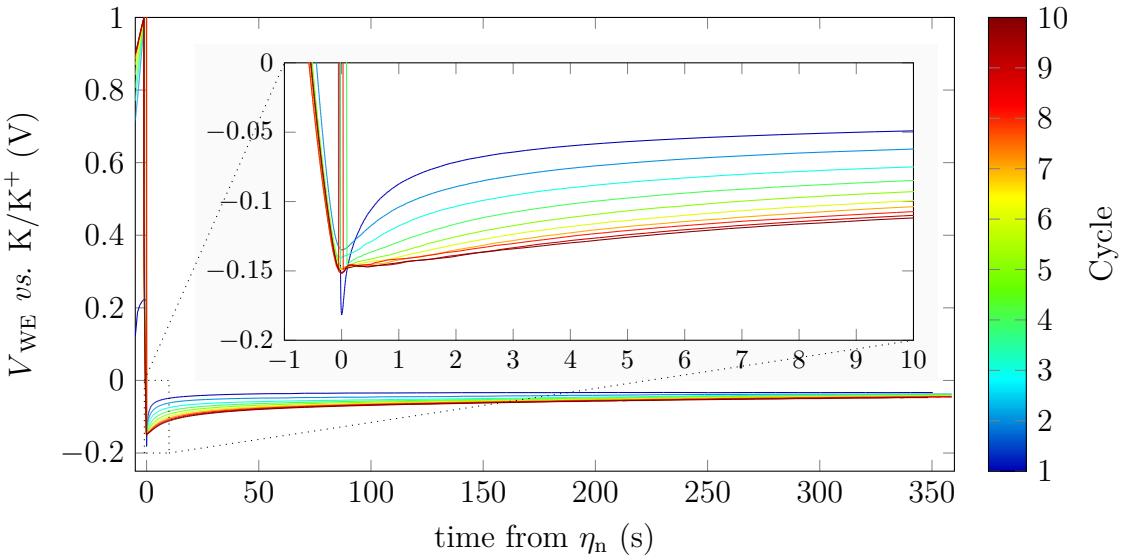


Figure 5.8: K nucleation peaks on Cu, from each cycle in fig. 5.7, overlaid for comparison.

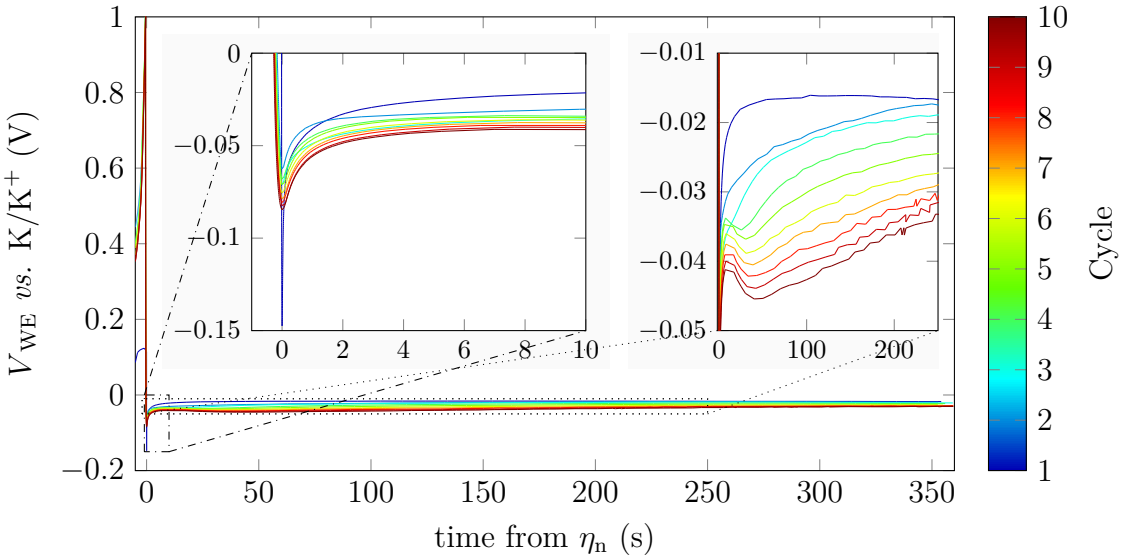


Figure 5.9: Overlaid nucleation and secondary peaks from each cycle for the first Au sample cycled at 0.36 mA cm^{-2} after a potentiostatic hold at 0.05 V for 15 min.

with such current densities or perhaps that Ag is much more potassiophilic, giving nucleation without a noticeable nucleation overpotential under favorable conditions.

Comparing the overpotential profiles in fig. 5.10, the peak of In_2O_3 is the most peculiar, as it is much shallower and broader than the rest. Au has the fastest nucleation. Ordering the peaks in terms of time to reach the nucleation overpotential, we get Au, Mg, Cu, W, In_2O_3. The fact that out of these, the four elements included in fig. 3.7 (Au, Mg, Cu, W) were ordered in the same way in terms of predicted potassiophilicity is compelling. However, looking at the data in figs. 5.11 and 5.15, there seems to be no such evident correlation in subsequent cycles.

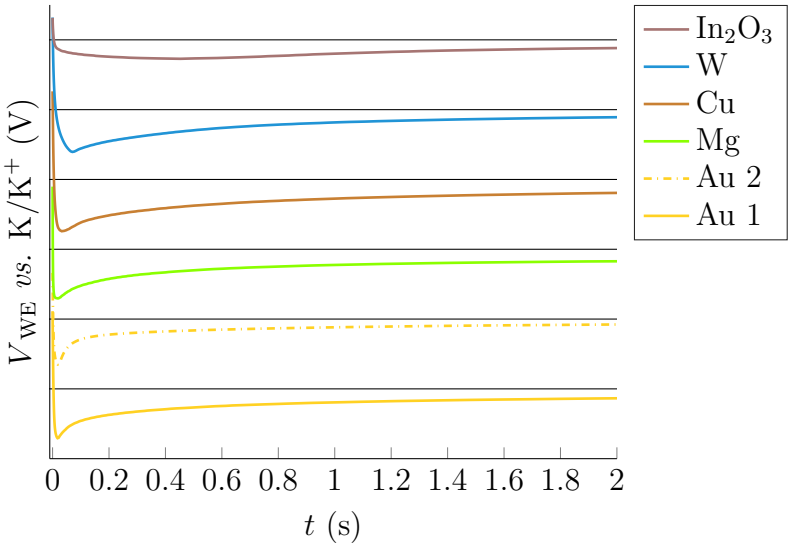


Figure 5.10: Nucleation peak for the first cycle at $0.36\,\mathrm{mA\,cm^{-2}}$ after a potentiostatic hold at 0.05 V. Data are vertically offset for clarity and the horizontal black lines correspond to voltages attained at the end of the half-cycle for each sample. The distance between two neighboring horizontal lines equals to 0.2 V.

Analyzing solely the depths of the nucleation peaks for each cycle, displayed in fig. 5.12, we see that the substrates no longer remain in the predicted order. Au and W, which would be expected to be on opposite sides given their $\Delta_{sol}H^{\infty}$, are close together near the middle, whereas Cu, which would be expected to be between them, has the deepest nucleation peaks. Cu exhibits both a deeper and wider nucleation peak compared to W, even though Cu was expected to be over 4 times less potassiophobic. If merely W were disregarded, however, the ordering would be restored, with shallower nucleation peaks corresponding to greater potassiophilicity. In_2O_3 being an outlier is consistent with the shallow peak in fig. 5.7, but is counter to the ordering in terms of time to nucleation overpotential.

Inspecting the FWHMs of the peaks in fig. 5.13, it can be seen that Au generally exhibits peaks an order of magnitude narrower than what is found for the other substrates. The 2nd peak of In_2O_3 is exceptionally broad, which is linked to its shallowness, seen in fig. 5.12.

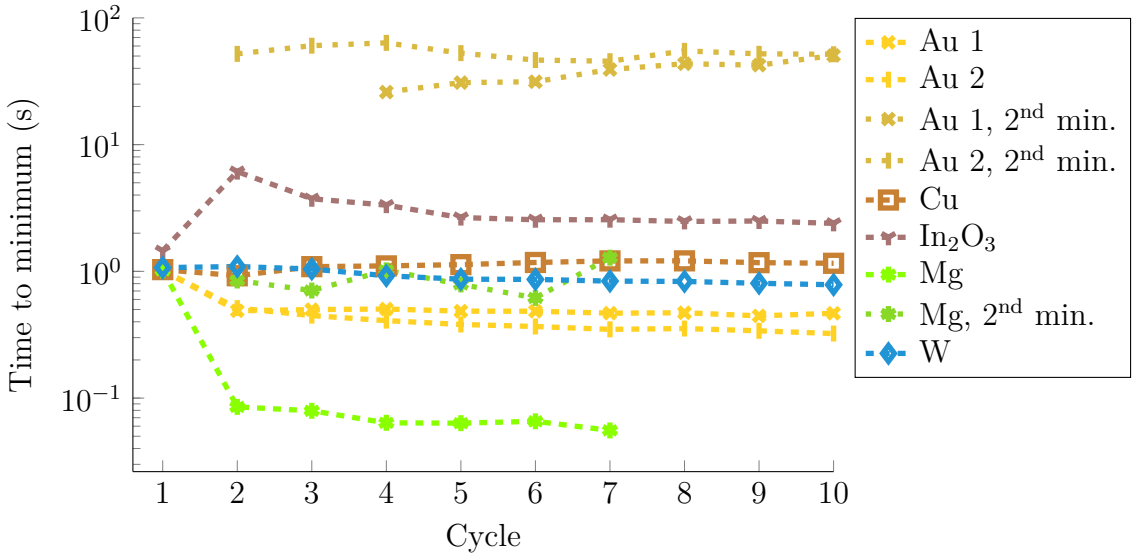


Figure 5.11: Time to nucleation in each cycle. In addition to the nucleation peaks, the secondary minima occurring in some of the Au and Mg cycles are included. *N.b.* the logarithmic y-axis. The reason the Mg plot only reaches the sixth cycle is that the cell soft-shorted. *Cf.* figs. 5.12 to 5.14 and 5.16.

The obtained coulombic efficiencies are presented in fig. 5.14. Discounting the first cycle, Mg has the overall lowest efficiency. Apart from Cu, W and one of the Au samples, global minima are attained at cycle 2.

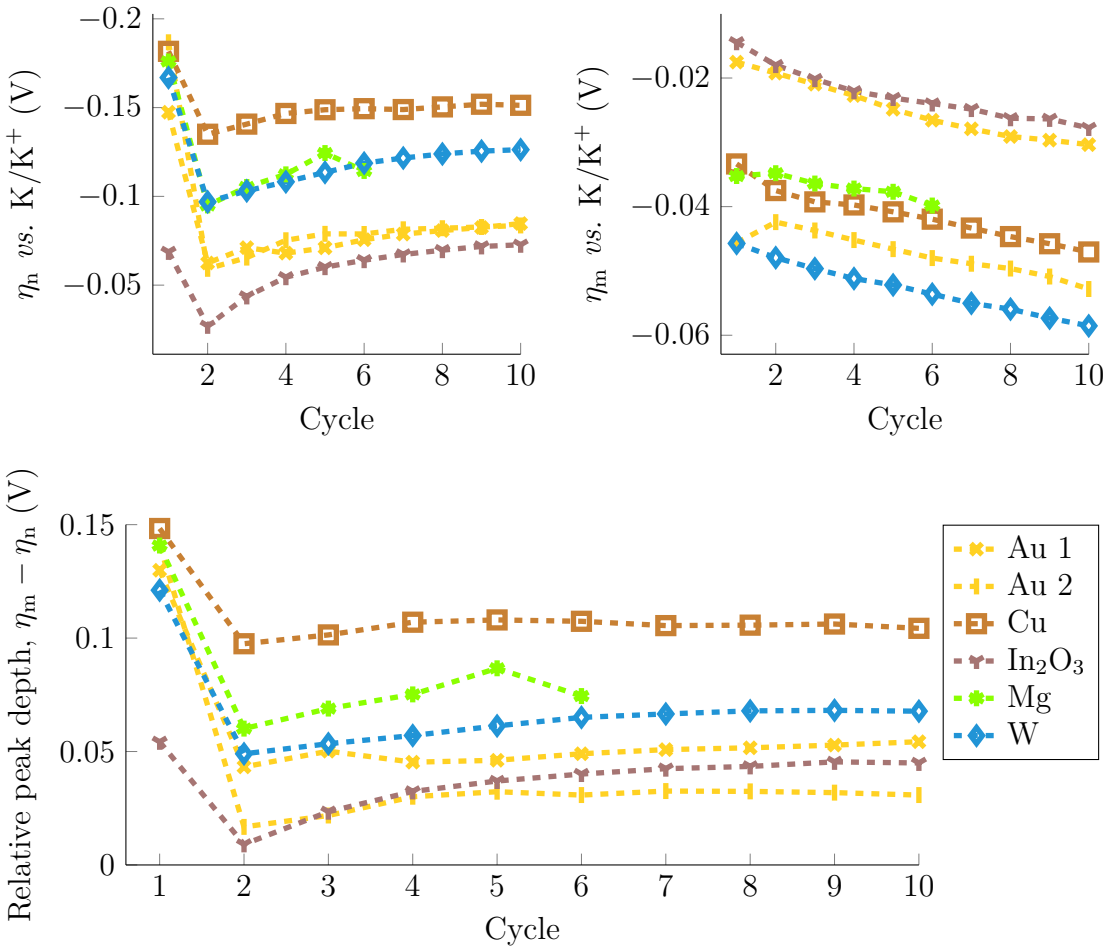


Figure 5.12: Absolute nucleation and minimum overpotentials for each cycle and the resulting relative depths of the nucleation peaks for the cycling at 0.36 mA cm^{-2} after a potentiostatic hold at 0.05 V. *N.b.* the reversed y-axis for η_n. The reason the Mg plot only reaches the sixth cycle is that the cell soft-shorted. *Cf.* figs. 5.11, 5.13, 5.14 and 5.16.

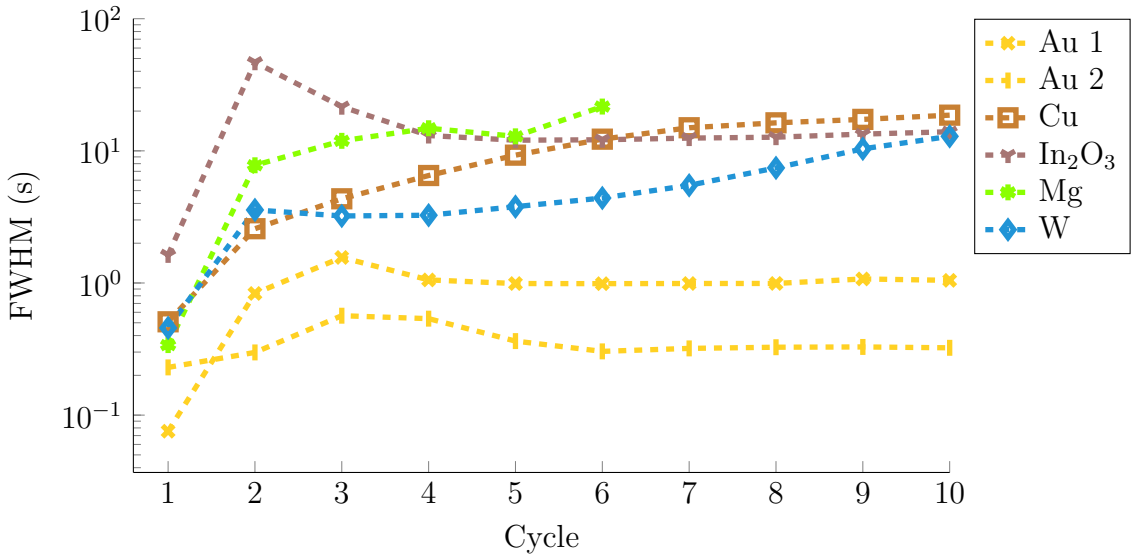


Figure 5.13: Full widths at half maxima of the nucleation peaks for the cycling at 0.36 mA cm^{-2} after a potentiostatic hold at 0.05 V. *N.b.* the logarithmic y-axis. The reason the Mg plot only reaches the sixth cycle is that the cell soft-shorted. *Cf.* figs. 5.11, 5.12, 5.14 and 5.17.

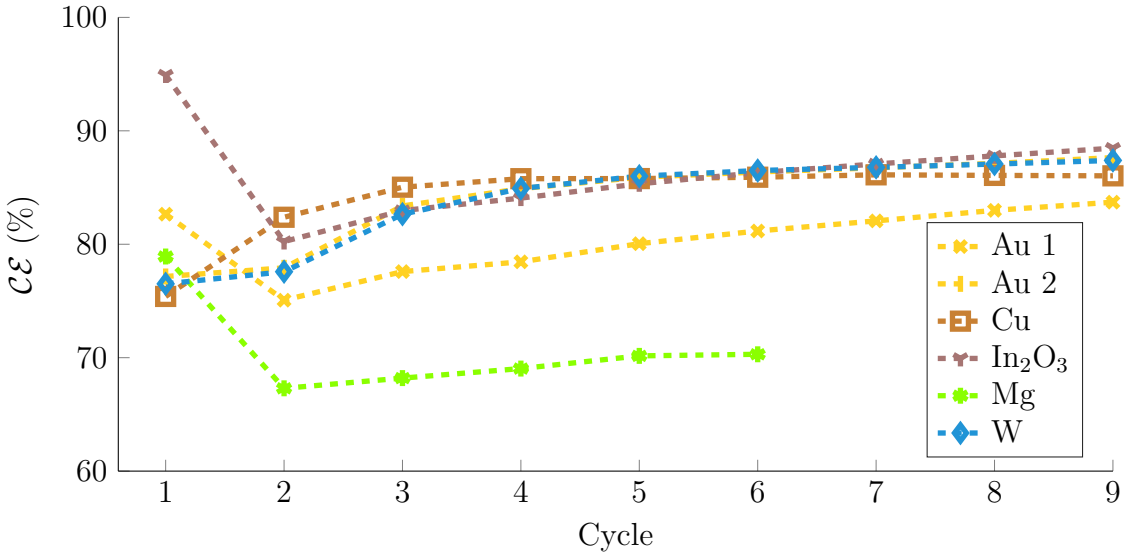


Figure 5.14: Coulombic efficiencies for the cycling at 0.36 mA cm^{-2} after a potentiostatic hold at 0.05 V. The reason the Mg plot only reaches the sixth cycle is that the cell soft-shorted. *Cf.* figs. 5.11 to 5.13 and 5.18.

5.2.2.1 Comparing with enthalpies of mixing

The data presented in figs. 5.11 to 5.14, combined with the $\Delta_{\text{sol}}H^{\infty}$ data in fig. 3.7 are presented in figs. 5.15 to 5.18. Since $\Delta_{\text{sol}}H^{\infty}$ for In_2O_3 with K was unknown, In_2O_3 data are excluded.

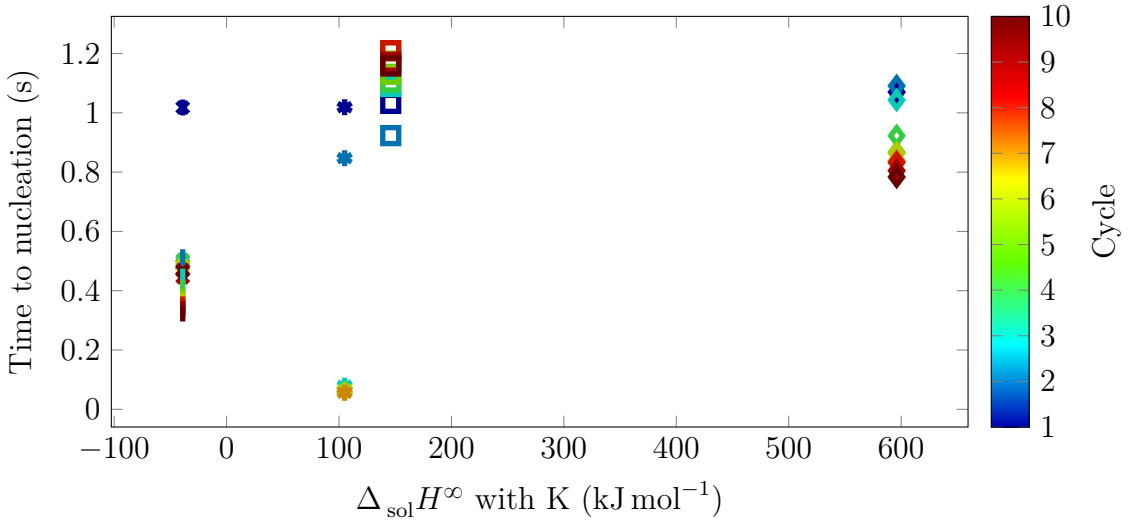


Figure 5.15: Time to nucleation, from fig. 5.11, in relation to enthalpies of mixing at infinite dilution in fig. 3.7.

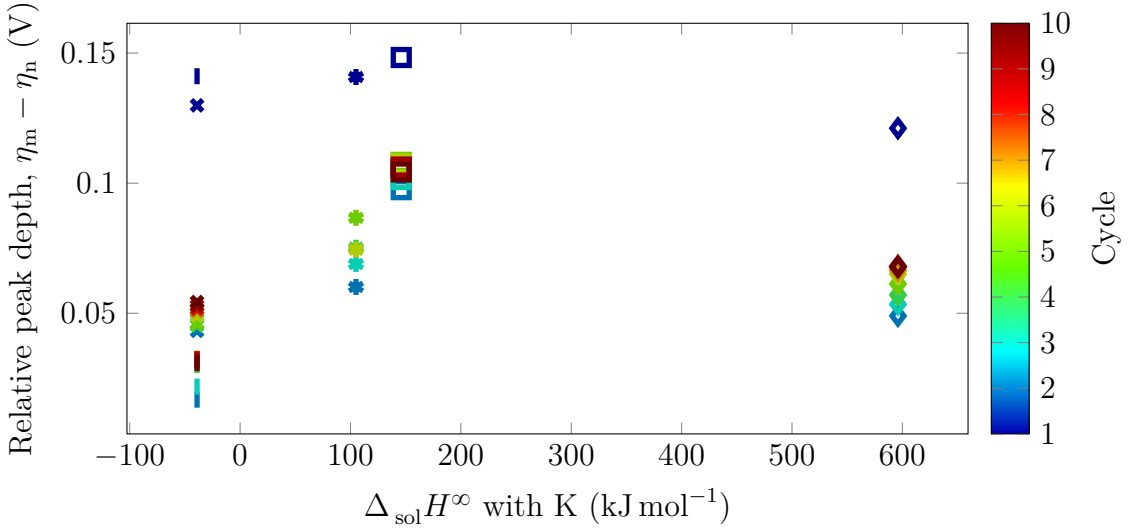


Figure 5.16: Relative peak depths, from fig. 5.12, in relation to enthalpies of mixing at infinite dilution in fig. 3.7. Corresponding figures for the absolute overpotentials η_{m} and η_{n} are included in appendix B.2.

As mentioned previously, there is no distinct correlation between $\Delta_{\text{sol}}H^{\infty}$ and the time to nucleation for all of the cycles. Excluding W, there is a clear correlation of $\Delta_{\text{sol}}H^{\infty}$ to peak depths and widths. No such correlation is readily apparent for the coulombic efficiency, however. As noted before, Mg is the clear outlier in this regard.

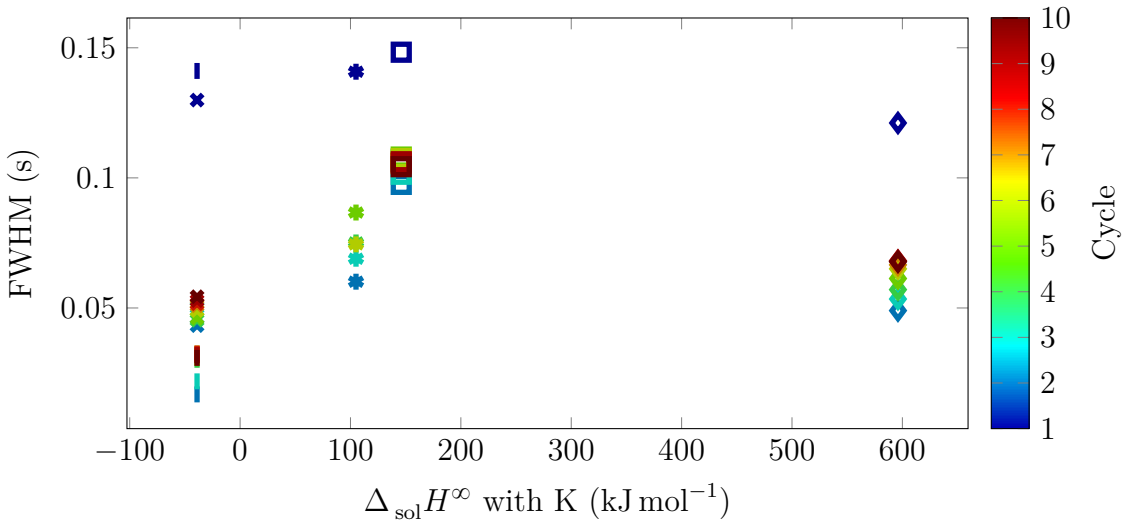


Figure 5.17: Peak widths, from fig. 5.13, in relation to enthalpies of mixing at infinite dilution in fig. 3.7.

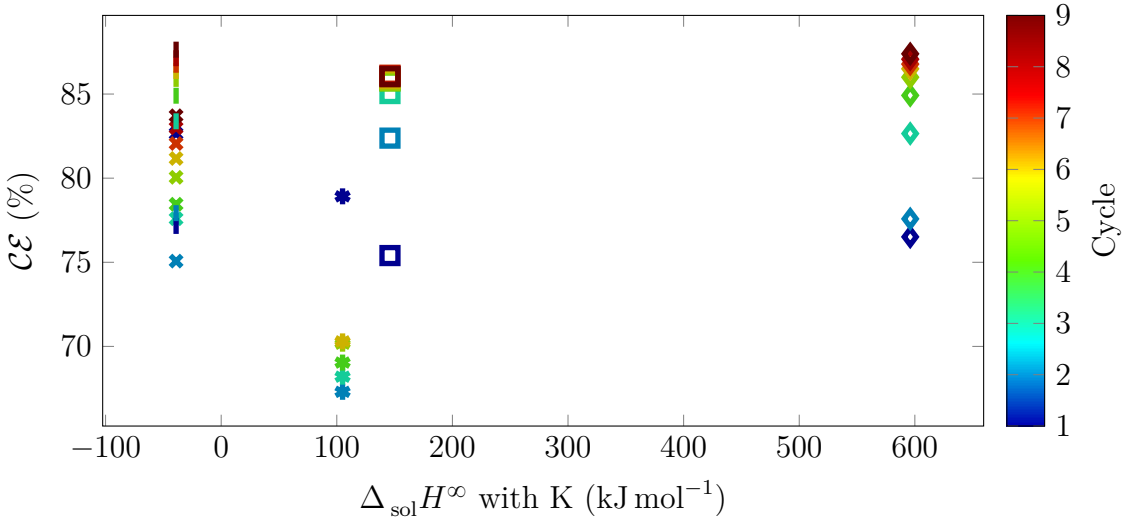


Figure 5.18: Coulombic efficiencies, from fig. 5.14, in relation to enthalpies of mixing at infinite dilution in fig. 3.7.

5.2.3 Discussion

As alluded to before, for the substrates sputtered onto Cu there was the possibility of delamination of the substrate from the bulk Cu, which could greatly affect the results. However, even if such delamination did occur for Au or Mg, their data are significantly distinct from both each other and Cu. Furthermore, oxide layers could have been formed on the less stable substrates, also affecting the nucleation process. Mg is especially prone to oxidation, but Cu also slowly forms an oxide layer when exposed to the atmosphere. In the context of electrochemistry, oxide films may form even on noble metals, such as Au [27].

Apparently other researchers also have had major problems with cyclic voltammetry using Fc in DME before, so it might be a topic worth exploring further separately. It is regrettable that so many cells resulted in failure, as the variety of substrates in the last experiments was limited. I would especially have liked to have a fully functioning Ag cell for the final comparisons. With several more samples, a statistically significant relation between peak features and $\Delta_{\text{sol}}H^{\infty}$ could potentially have been determined.

6

Conclusion

The need to employ separate reference electrodes was demonstrated and the suitability of K as a reference for studying K nucleation examined with cyclic voltammetry. Cells with K exhibit a stepwise voltage response $V_{\mathrm{WE-CE}}$ due to a shift in potential of the K electrode. The shift is absent from the first cycle and occurs only from the 2$^{\mathrm{nd}}$ cycle onwards. We suspect that the potential steps correspond to stripping freshly deposited K *vs.* pitting from the bulk K, as there is only the bulk K in the first cycle.

Cells with a range of substrates, some of which were predicted to have a certain potassiophilicity, were cycled galvanostatically. A prior potentiostatic step for SEI formation is beneficial, giving rise to more pronounced nucleation peaks. A measure of time to the nucleation overpotential, as well as nucleation peak depths and widths mostly support these predictions, although not exactly. There is evidence that W, which was predicted to be exceedingly potassiophobic, might be less so than both Cu and Mg. Ag may also be more potassiophilic than Au, which was also unexpected. Due to the limited sample size and high cell failure rate it would be worthwhile to replicate these experiments with an expanded roster of substrates, along with more samples of each.

Bibliography

[1] Rystad Energy. *Powering up: Global battery demand to surge by 2030, supply headaches on the horizon*. Mar. 2022. URL: https://www.rystadenergy.com/newsevents/news/press-releases/powering-up-global-battery-demand-to-surge-by-2030-supply-headaches-on-the-horizon/ (visited on 05/24/2022).

[2] Reuters. *Global lithium-ion battery capacity may rise five-fold by 2030 - Wood Mackenzie*. Mar. 2022. URL: https://www.reuters.com/business/autos-transportation/global-lithium-ion-battery-capacity-may-rise-five-fold-by-2030-wood-mackenzie-2022-03-22/ (visited on 05/24/2022).

[3] The Cambridge Crystallographic Data Centre. *Deposition Number 1700234, ICSD Entry: 191311*. Feb. 2018. URL: https://www.ccdc.cam.ac.uk/structures/Search?Ccdcid=1700234 (visited on 08/15/2022).

[4] FIZ Karlsruhe. *Struct. formula Li C6, Collection Code 191311*. Inorganic Crystal Structure Database. 2014.

[5] O. Dolotko *et al.* "Understanding structural changes in NMC Li-ion cells by *in situ* neutron diffraction". In: *Journal of Power Sources* 255 (2014), pp. 197–203. ISSN: 0378-7753. DOI: 10.1016/j.jpowsour.2014.01.010.

[6] Kai Yan *et al.* "Selective deposition and stable encapsulation of lithium through heterogeneous seeded growth". In: *Nature Energy* 1.3 (2016). DOI: 10.1038/nenergy.2016.10.

[7] Simeng Zhang *et al.* "Phase Diagram Determined Lithium Plating/Stripping Behaviors on Lithiophilic Substrates". In: *ACS Energy Letters* 6.11 (2021), pp. 4118–4126. DOI: 10.1021/acsenergylett.1c02127.

[8] Y. Marcus. "Thermodynamic functions of transfer of single ions from water to nonaqueous and mixed solvents: Part 3 - Standard potentials of selected electrodes". In: *Pure and Applied Chemistry* 57.8 (1985), pp. 1129–1132. DOI: 10.1351/pac198557081129.

[9] U.S. Geological Survey. *Lithium*. Tech. rep. Jan. 2021. URL: https://pubs.usgs.gov/periodicals/mcs2021/mcs2021-lithium.pdf.

[10] Yangyang Liu *et al.* "Insight into the critical role of exchange current density on electrodeposition behavior of lithium metal". In: *Advanced Science* 8.5 (2021), p. 2003301. DOI: 10.1002/advs.202003301.

[11] Kevin N. Wood, Malachi Noked & Neil P. Dasgupta. "Lithium Metal Anodes: Toward an Improved Understanding of Coupled Morphological, Electrochemical, and Mechanical Behavior". In: *ACS Energy Letters* 2.3 (2017), pp. 664–672. DOI: 10.1021/acsenergylett.6b00650.

[12] Matthew Sadd. "*Operando* Analysis of Materials and Processes in Next Generation Batteries, Analytical Methods Revealing the Operating Mechanisms of Next Generation Battery Chemistries". PhD thesis. Chalmers University of Technology, 2021. ISBN: 978-91-7905-608-7. URL: https://research.chalmers.se/publication/527824.

[13] Norio Takenaka *et al.* "Frontiers in Theoretical Analysis of Solid Electrolyte Interphase Formation Mechanism". In: *Advanced Materials* 33.37 (2021), p. 2100574. DOI: 10.1002/adma.202100574.

[14] E. Peled & S. Menkin. "Review—SEI: Past, Present and Future". In: *Journal of The Electrochemical Society* 164.7 (2017), A1703–A1719. DOI: 10.1149/2.1441707jes.

[15] Elif Ceylan Cengiz *et al.* "Review—reference electrodes in Li-ion and next generation batteries: Correct potential assessment, applications and practices". In: *Journal of The Electrochemical Society* 168.12 (2021), p. 120539. DOI: 10.1149/1945-7111/ac429b.

[16] Prayag Biswal *et al.* "Nucleation and Early Stage Growth of Li Electrodeposits". In: *Nano Letters* 19.11 (2019). PMID: 31566985, pp. 8191–8200. DOI: 10.1021/acs.nanolett.9b03548.

[17] Prayag Biswal *et al.* "The early-stage growth and reversibility of Li electrodeposition in Br-rich electrolytes". In: *Proceedings of the National Academy of Sciences* 118.2 (2021), e2012071118. DOI: 10.1073/pnas.2012071118.

[18] Noémie Elgrishi *et al.* "A Practical Beginner's Guide to Cyclic Voltammetry". In: *Journal of Chemical Education* 95.2 (2018), pp. 197–206. DOI: 10.1021/acs.jchemed.7b00361.

[19] Nataliia Mozhzhukhina & Ernesto J. Calvo. "Perspective—The Correct Assessment of Standard Potentials of Reference Electrodes in Non-Aqueous Solution". In: *Journal of The Electrochemical Society* 164.12 (2017), A2295–A2297. DOI: 10.1149/2.0341712jes.

[20] Ethan Ho & National Institute of Standards and Technology, U.S. Department of Commerce. *Ferrocene*. NIST Chemistry WebBook, Standard Reference Database Number 69. Aug. 2014. DOI: 10.18434/T4D303. URL: https://webbook.nist.gov/cgi/cbook.cgi?ID=C102545.

[21] Peter M. Attia. *Cyclic voltammetry simulation tutorials*. URL: https://petermattia.com/cyclic_voltammetry_simulation (visited on 06/26/2022).

[22] Wei Liu, Pengcheng Liu & David Mitlin. "Tutorial review on structure – dendrite growth relations in metal battery anode supports". In: *Chemical Society Reviews* 49.20 (2020), pp. 7284–7300. DOI: 10.1039/d0cs00867b.

[23] Tomooki Hosaka *et al.* "Potassium Metal as Reliable Reference Electrodes of Nonaqueous Potassium Cells". In: *The Journal of Physical Chemistry Letters* 10.12 (2019). PMID: 31042388, pp. 3296–3300. DOI: 10.1021/acs.jpclett.9b00711.

[24] G. Gritzner & J. Kůta. "Recommendations on reporting electrode potentials in nonaqueous solvents: IUPC commission on electrochemistry". In: *Electrochimica Acta* 29.6 (1984), pp. 869–873. ISSN: 0013-4686. DOI: 10.1016/0013-4686(84)80027-4.

[25] Thrinathreddy Ramireddy *et al.* "Insights into Electrochemical Behavior, Phase Evolution and Stability of Sn upon K-alloying/de-alloying via In Situ Studies". In: *Journal of The Electrochemical Society* 164.12 (2017), A2360–A2367. DOI: 10.1149/2.0481712jes.

[26] William M. Haynes, David R. Lide & Thomas J. Bruno. *CRC Handbook of Chemistry and Physics: A ready-reference book of Chemical and physical data.* CRC Press, 2016.

[27] B.E. Conway. "Electrochemical oxide film formation at noble metals as a surface-chemical process". In: *Progress in Surface Science* 49.4 (1995), pp. 331–452. ISSN: 0079-6816. DOI: 10.1016/0079-6816(95)00040-6.

[28] Bruno Scrosati *et al.*, eds. *Lithium Batteries: Advanced Technologies and Applications.* The ECS Series of Texts and Monographs. Hoboken, NJ: Wiley-Blackwell, June 2013. ISBN: 978-1-118-18365-6.

A

Calculations of theoretical capacities of anode materials

It is important to note that the following calculations only consider the anode materials and do not provide the specific capacities of any full cells.

A.1 Pure lithium

Assuming complete efficiency, Li can provide one elementary unit of charge per atom. Thus, we simply can calculate

$$\frac{e}{m_{\mathrm{Li}}} = \frac{1.602\,176\,634 \times 10^{-19}\,\mathrm{C}}{6.94\,\mathrm{u}} \approx 3861\,\mathrm{mA\,h\,g^{-1}}, \tag{A.1}$$

where e is the elementary charge and m_{Li} is the atomic mass of lithium.

A.2 Lithium intercalated in graphite

In conventional graphite anodes, there are at least 6 carbon (C) atoms per Li [28], so eq. (A.1) only needs to be slightly modified, giving

$$\frac{e}{6m_{\mathrm{C}}} = \frac{1.602\,176\,634 \times 10^{-19}\,\mathrm{C}}{6 \times 12.011\,\mathrm{u}} \approx 371.9\,\mathrm{mA\,h\,g^{-1}}, \tag{A.2}$$

where m_{C} is the atomic mass of carbon. Note that this calculation is for graphite before lithiation, so the mass of the lithium is not relevant here. This mass would also need to be accounted for in a calculation for a full cell.

A.3 Potassium intercalated in graphite

The calculation is similar to eq. (A.2), however 1 : 8 is the maximum ratio of K : C. This gives

$$\frac{e}{8m_{\mathrm{C}}} = \frac{1.602\,176\,634 \times 10^{-19}\,\mathrm{C}}{8 \times 12.011\,\mathrm{u}} \approx 278.93\,\mathrm{mA\,h\,g^{-1}}. \tag{A.3}$$

Similarly to before, this calculation is for graphite prior to potassiation. Even with an otherwise equivalent cathode to the one in the Li case, the specific capacity of the cathode would also suffer due to the difference in atomic weights between Li and K.

A.4 Pure sodium

As in appendix A.1, but with the atomic mass of sodium instead, we get

$$\frac{e}{m_{\mathrm{Na}}} = \frac{1.602\,176\,634 \times 10^{-19}\,\mathrm{C}}{22.989\,769\,28\,\mathrm{u}} \approx 1165.8\,\mathrm{mA\,h\,g^{-1}}. \tag{A.4}$$

A.5 Pure potassium

As in appendix A.1, but with the atomic mass of potassium instead, we get

$$\frac{e}{m_{\mathrm{K}}} = \frac{1.602\,176\,634 \times 10^{-19}\,\mathrm{C}}{39.0983\,\mathrm{u}} \approx 685.5\,\mathrm{mA\,h\,g^{-1}}. \tag{A.5}$$

B

Supplementary measurement data

B.1 Nucleation peak shapes

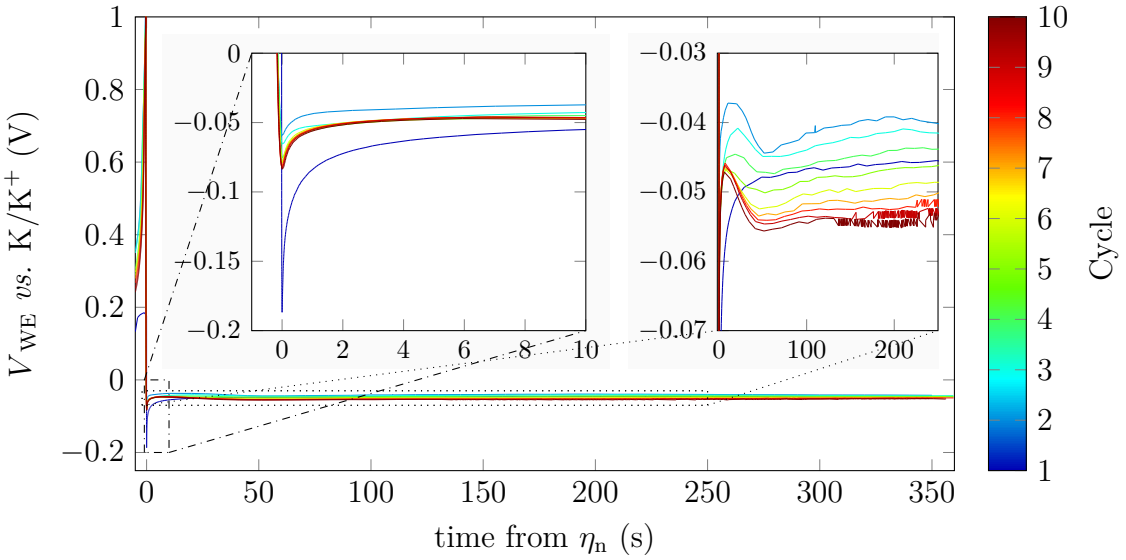


Figure B.1: Overlaid nucleation peaks for the 2$^{\mathrm{nd}}$ Au sample cycled at 0.36 mA cm^{-2} after a potentiostatic hold at 0.05 V for 15 min, together with secondary peaks.

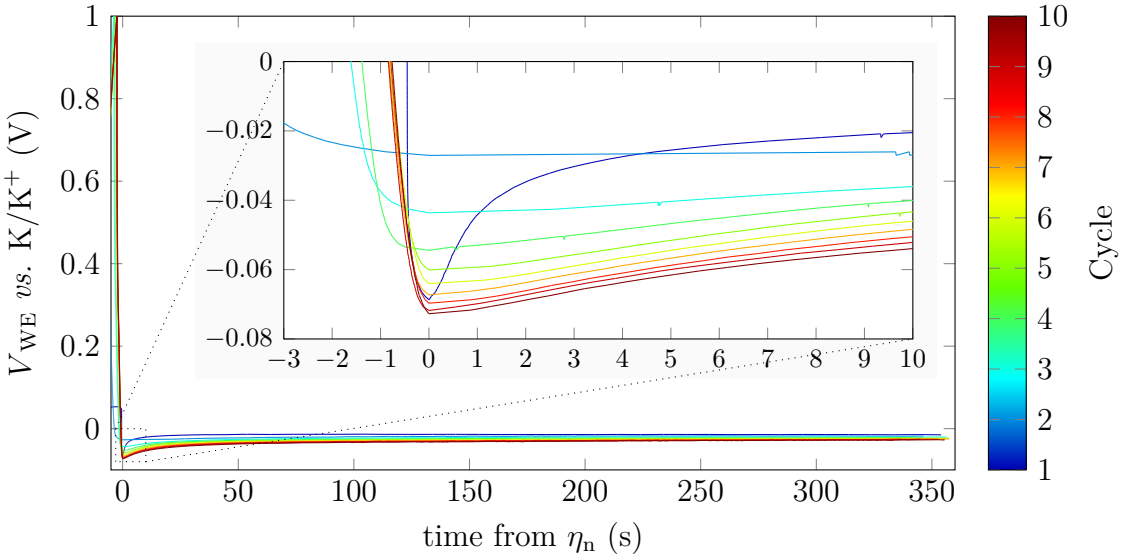


Figure B.2: Overlaid nucleation peaks for the In_2O_3 sample cycled at 0.36 mA cm^{-2} after a potentiostatic hold at 0.05 V for 15 min.

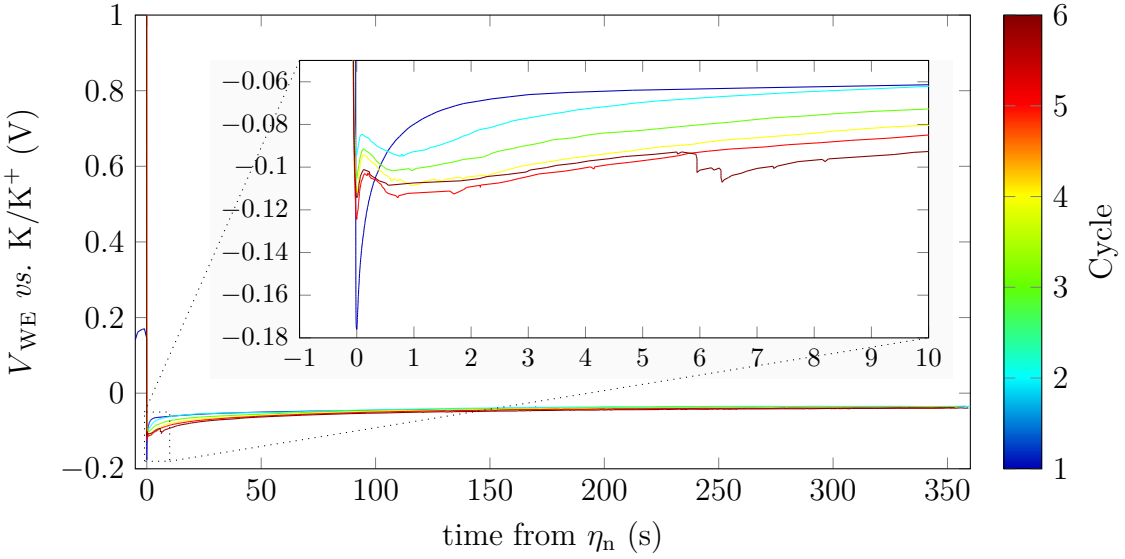


Figure B.3: Overlaid nucleation peaks for the first 6 cycles of the Mg sample cycled at 0.36 mA cm^{-2} after a potentiostatic hold at 0.05 V for 15 min. The remaining cycles are omitted due to cell failure in the 7$^{\mathrm{th}}$ cycle. *N.b.* that the secondary minimum is deeper than the first, but only in the 2$^{\mathrm{nd}}$ cycle.

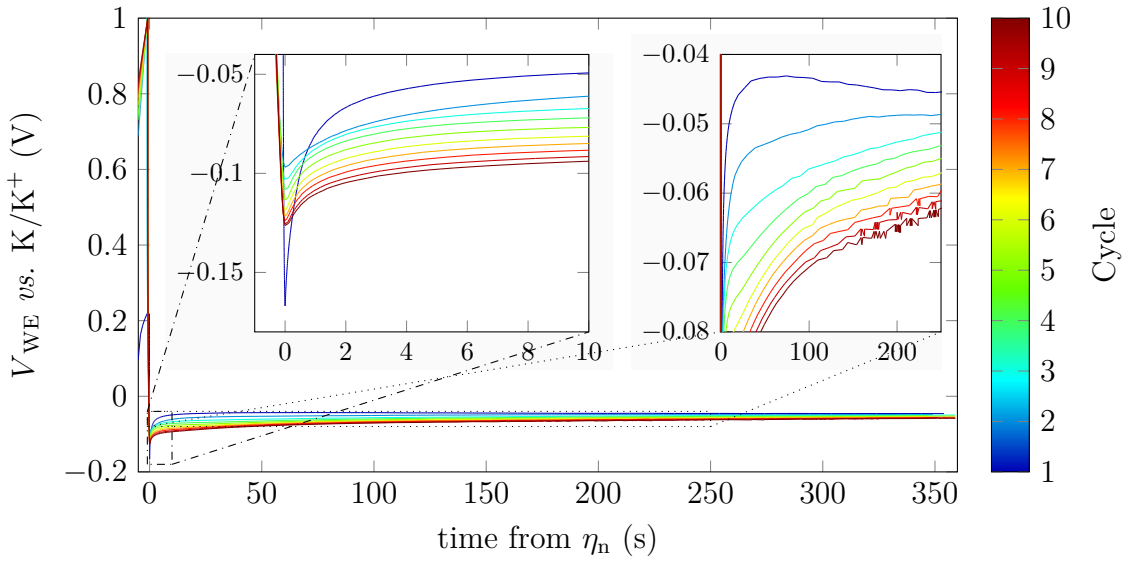


Figure B.4: Overlaid nucleation peaks for the W sample cycled at 0.36 mA cm^{-2} after a potentiostatic hold at 0.05 V for 15 min.

B.2 Absolute overpotentials *vs.* $\Delta_{\mathrm{sol}}H^{\infty}$

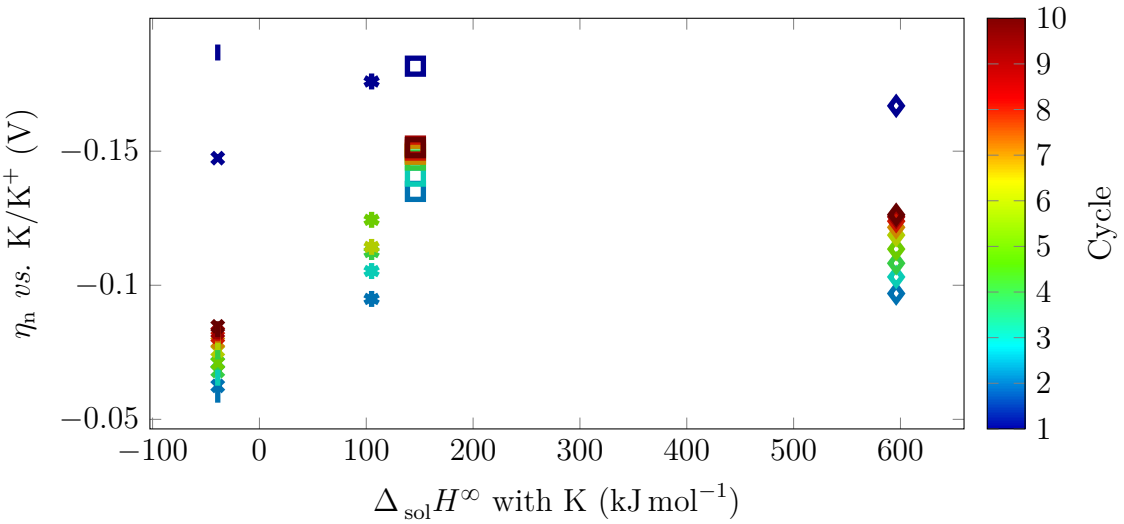


Figure B.5: Absolute nucleation overpotentials from fig. 5.12 in relation to enthalpies of mixing at infinite dilution in fig. 3.7. *N.b.* the reversed y-axis.

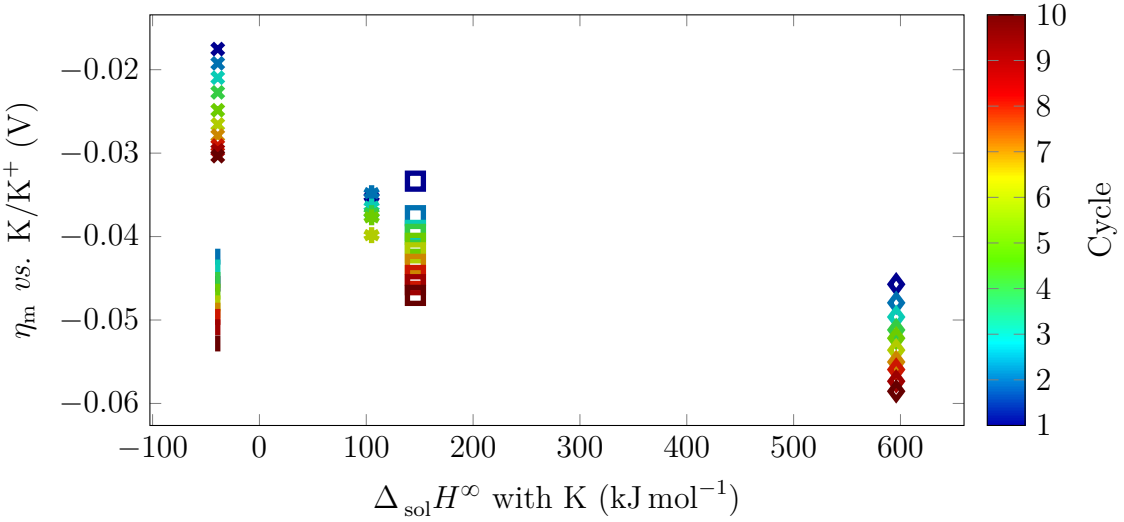


Figure B.6: Absolute η_{m}s from fig. 5.12 in relation to enthalpies of mixing at infinite dilution in fig. 3.7.

DEPARTMENT OF MATERIALS PHYSICS
CHALMERS UNIVERSITY OF TECHNOLOGY
Gothenburg, Sweden
www.chalmers.se



CHALMERS
UNIVERSITY OF TECHNOLOGY